

# A NUMERICAL SCHEME FOR THREE-DIMENSIONAL FRONT PROPAGATION AND CONTROL OF JORDAN MODE

K. R. ARUN

**ABSTRACT.** We study the propagation of a three-dimensional weakly nonlinear wavefront into a polytropic gas in a uniform state and at rest. The successive positions and geometry of the wavefront are obtained by solving the conservation form of equations of a weakly nonlinear ray theory. The proposed set of equations forms a weakly hyperbolic system of seven conservation laws with an additional vector constraint analogous to the scalar solenoidal condition in the equations of ideal magnetohydrodynamics. The new divergence-free type constraint is termed as geometric solenoidal constraint. The analysis of a Cauchy problem for the linearised system shows that when this constraint is satisfied initially, the solution does not exhibit any Jordan mode. For the numerical simulation of the conservation laws we employ a high resolution central scheme. The second order accuracy of the scheme is achieved by using MUSCL type reconstructions and Runge-Kutta time discretisations. A constrained transport technique is used to enforce the geometric solenoidal constraint. The results of several numerical experiments are presented which confirm the efficiency and robustness of the proposed numerical method and the control of Jordan mode.

## 1. INTRODUCTION

The propagation of a curved nonlinear wavefront exhibits a very complex phenomenon of possessing curves of discontinuity (singularities), called kinks [29], across which the normal to the front and the amplitude distribution on it are discontinuous. Such a wavefront, say one from the succession of wavefronts produced by a piston, may interact with a shock front and disappear from the flow field. However, there will always be a continuous train of wavefronts behind the shock front and we strongly believe that the geometry of a nonlinear wavefront is qualitatively similar to that of a weak shock. Experimental observations due to Sturtevant and Kulkarny [37] and analytical and numerical investigations due to Whitham and his collaborators [18, 34, 35, 38, 39] using geometrical shock dynamics (GSD) show that a moderately weak shock front becomes non-smooth with kinks during its evolution.

The differential equations of evolution of a nonlinear wavefront or a shock front in a gaseous medium in terms of rays and propagation laws have been available for a long time [28], see also [29, 30] for historical details. However, the formation of singularities on these fronts necessitates the conservative formulation of the governing equations. The conservation form of the equations of evolution of a surface in any space dimensions is known as kinematical conservation laws (KCL). The KCL is a pure geometric result, and hence, it does not take into consideration any dynamics of the propagating surface. This makes the KCL an incomplete system. The closure relations for KCL can be derived by considering the dynamical conditions of the propagating surface. The KCL for a curve evolving in two-dimensional (2-D) space  $\mathbb{R}^2$ , known as 2-D KCL, was first obtained by Morton, Prasad and Ravindran [26]. Later, Prasad and his collaborators extensively used the 2-D KCL along with suitable closure equations derived on physical considerations to solve several

---

*Date:* December 29, 2010.

*2000 Mathematics Subject Classification.* Primary 35L60, 35L65, 35L67, 35L80; Secondary 58J47, 65M06.

*Key words and phrases.* kinematical conservation laws, kink, ray theory, weakly nonlinear wavefront, polytropic gas, mean curvature.

interesting problems, see [6, 7, 8, 25, 30, 31] for more details. The three-dimensional (3-D) KCL, a system of six conservation laws, for a surface evolving in 3-D space  $\mathbb{R}^3$  were first derived by Giles, Prasad and Ravindran [17] and later on analysed by Arun and Prasad [3, 4]. The closure relation for 3-D KCL for a weakly nonlinear wavefront, representing the energy propagation along the rays of a weakly nonlinear ray theory (WNLRT) [28, 29], was put in an appropriate conservation form by Arun and Prasad [3]. The 3-D KCL with the transport equation of WNLRT gives a complete set of seven equations in conservation form governing the evolution of a 3-D nonlinear wavefront in a polytropic gas.

The system of seven conservation laws obtained by appending the transport equation of WNLRT to 3-D KCL has been referred to as the conservation laws of 3-D WNLRT. This system also contains a vector constraint, each of whose three components is analogous to the solenoidal constraint in the equations of ideal magnetohydrodynamics. We shall refer to this new divergence-free type condition as ‘geometric solenoidal constraint’. It has been proved in [3, 4] that the system of conservation laws of 3-D WNLRT is only weakly hyperbolic, in the sense the system has a multiple eigenvalue with an incomplete eigenspace. The appearance of  $\delta$ -waves,  $\delta$ -shocks and Jordan modes in the solution of such systems generally makes the numerical approximation of weakly hyperbolic systems very complex, see [12, 14, 23]. Another major challenge in the numerical modelling of 3-D WNLRT is that a numerical approximation of the system of conservation laws may not respect the geometric solenoidal constraint.

The goal of the present work is to analyse a Cauchy problem for the conservation laws of 3-D WNLRT and present the results of extensive numerical simulations of the conservation laws. It is well known from the literature that the solution to a Cauchy problem for a weakly hyperbolic system typically contains a mode which grows polynomially in time. This mode, the so called Jordan mode, is in the direction of the generalised eigenvector. However, such a mode does not arise in the case of certain systems with stationary differential constraints, see [9, 10, 11, 27] for more details. Due to the complexity of the system of equations of 3-D WNLRT, it is difficult to establish this result for the full nonlinear system. Therefore, we first linearise the equations of 3-D WNLRT and show that if the geometric solenoidal constraint is satisfied at  $t = 0$ , then the Jordan mode of this weakly hyperbolic system (which grows linearly with  $t$ ) does not appear in the solution of the linear system. We strongly believe this to be true also for the full nonlinear equations of the 3-D WNLRT. In [2] we have reported some preliminary numerical investigations on 3-D WNLRT using staggered central schemes. The results in [2] clearly show the efficacy of 3-D WNLRT to produce several geometrical features of nonlinear wavefronts. However, it well known that the staggered central schemes suffer from a large amount numerical diffusion and they have a lesser stability range, see [22]. Therefore, in this paper we employ the high-resolution central scheme of Kurganov and Tadmor (KxT) [22] for the numerical simulation of the conservation laws of 3-D WNLRT. A main advantage of the KxT scheme is that it admits a semi-discrete formulation, and hence it is very easy to achieve any high order accuracy in space and time using standard recovery procedures and TVD Runge-Kutta time stepping procedures. Like other central schemes, the KxT scheme also has the advantage that it does not require complicated and time consuming Riemann solvers. This is particularly important, as the conservations laws of 3-D WNLRT are not strictly hyperbolic and system is in multi-dimensions, where there is no exact Riemann solver. However, the high resolution central scheme need not respect the geometric solenoidal constraint and therefore we use a constrained transport technique to enforce it. Our numerical experiments confirm the efficiency and robustness of the numerical method and we verify that constrained transport technique preserves the constraint up to machine round off error. The numerical results reveal many fascinating geometrical features of 3-D nonlinear wavefronts and the non-appearance of Jordan mode.

## 2. GOVERNING EQUATIONS

Consider a one parameter family of surfaces in  $(x_1, x_2, x_3)$ -space such that it represents the successive positions of a moving surface  $\Omega_t$  as time varies. Associated with the family, we have a ray velocity  $\boldsymbol{\chi}$  at any point  $(x_1, x_2, x_3)$  on the surface  $\Omega_t$ . We consider only the isotropic evolution of  $\Omega_t$  so that we take  $\boldsymbol{\chi}$  to be in the direction of the unit normal  $\mathbf{n}$  to  $\Omega_t$ , i.e.  $\boldsymbol{\chi} = m\mathbf{n}$ , where  $m$  is the normal velocity of propagation of  $\Omega_t$ . We introduce a ray coordinate system  $(\xi_1, \xi_2, t)$  such that  $t = \text{const}$  is  $\Omega_t$  with  $\xi_1, \xi_2$  as the surface coordinates. Further,  $\xi_1 = \text{const}$ ,  $\xi_2 = \text{const}$  represent the rays, i.e. a two parameter family of curves orthogonal to  $\Omega_t$ . Let  $\mathbf{u}$  and  $\mathbf{v}$  be unit tangent vectors to the curves  $\xi_2 = \text{const}$  and  $\xi_1 = \text{const}$  on  $\Omega_t$ , respectively and let  $\mathbf{n}$  be the unit normal to  $\Omega_t$ . Then we have

$$(2.1) \quad \mathbf{n} = \frac{\mathbf{u} \times \mathbf{v}}{\|\mathbf{u} \times \mathbf{v}\|}.$$

Let an element of distance along a curve  $\xi_2 = \text{const}, t = \text{const}$  be  $g_1 d\xi_1$ . Analogously, denote by  $g_2 d\xi_2$ , the element of distance along a curve  $\xi_1 = \text{const}, t = \text{const}$  and by  $mdt$ , the element of distance along a ray  $\xi_1 = \text{const}, \xi_2 = \text{const}$ . Based on geometrical considerations we can derive the 3-D KCL [3, 17]

$$(2.2) \quad (g_1 \mathbf{u})_t - (m\mathbf{n})_{\xi_1} = 0,$$

$$(2.3) \quad (g_2 \mathbf{v})_t - (m\mathbf{n})_{\xi_2} = 0$$

subject to the condition

$$(2.4) \quad (g_2 \mathbf{v})_{\xi_1} - (g_1 \mathbf{u})_{\xi_2} = 0.$$

For many important properties of (2.2)-(2.4) we refer the reader to [3]. From (2.2)-(2.3) we can show that the quantity  $(g_2 \mathbf{v})_{\xi_1} - (g_1 \mathbf{u})_{\xi_2}$  does not depend on  $t$ . Existence of coordinates  $\xi_1$  and  $\xi_2$  on  $\Omega_0$  guarantees that the condition (2.4) is satisfied at  $t = 0$ . Clearly, (2.2)-(2.3) imply that (2.4) is satisfied for all  $t$ . In other words, this constraint is inherent to the set of equations (2.2)-(2.3), i.e. once fulfilled at the initial time, it is fulfilled for all times. It is very interesting to note that the constraint (2.4) is analogous to the solenoidal condition in the equations of ideal magnetohydrodynamics. To see this, let us introduce three vectors  $\mathfrak{B}_k, k = 1, 2, 3$ , in  $\mathbb{R}^2$  via

$$(2.5) \quad \mathfrak{B}_k := (g_2 v_k, -g_1 u_k).$$

Using this definition of  $\mathfrak{B}_k$ , (2.4) can be recast in an equivalent form

$$(2.6) \quad \text{div}(\mathfrak{B}_k) = 0, \quad k = 1, 2, 3.$$

Therefore, we infer that all the three vectors  $\mathfrak{B}_k$  are divergence-free at any time  $t$  if they are so at time  $t = 0$ . Note that there are three scalar constraints in (2.6) analogous to the solenoidal condition in the equations of two-dimensional ideal magnetohydrodynamics. We shall refer to (2.4) (or (2.6)), as ‘geometric solenoidal constraint’.

The 3-D KCL is a system of six scalar evolution equations (2.2)-(2.3). It has to be, however, noted that  $\|\mathbf{u}\| = \|\mathbf{v}\| = 1$  and there are seven dependent variables in (2.2)-(2.3): two independent components of each of  $\mathbf{u}$  and  $\mathbf{v}$ , the front velocity  $m$  of  $\Omega_t$  and  $g_1$  and  $g_2$ . Thus, KCL is an under-determined system and can be closed only with the help of additional relations or equations, which would follow from the nature of the surface  $\Omega_t$  and the dynamics of the medium in which it propagates. Following [2, 3] we use the closure equation by considering the energy propagation along rays of WNLRT, see [29] for a comprehensive treatment of WNLRT. The energy transport equation of WNLRT for a polytropic gas initially at rest and in uniform state can be written in the

conservation form [3]

$$(2.7) \quad \left( (m-1)^2 e^{2(m-1)} g_1 g_2 \sin \chi \right)_t = 0,$$

where  $\chi$  is the angle between the vectors  $\mathbf{u}$  and  $\mathbf{v}$ . The system of equations (2.2)-(2.3) and (2.7) is the complete set of conservation laws of 3-D WNLRT describing the evolution of a nonlinear wavefront  $\Omega_t$ .

A quasilinear form of the system of equations (2.2)-(2.3) and (2.7) can be obtained as

$$(2.8) \quad AV_t + B^{(1)}V_{\xi_1} + B^{(2)}V_{\xi_2} = 0,$$

where  $V = (u_1, u_2, v_1, v_2, m, g_1, g_2)^T$ . The expressions for the matrices  $A, B^{(1)}$  and  $B^{(2)}$  are given in [3]. We would like to point out that the eigenvalues of the system (2.8) are  $\lambda_1, \lambda_2 (= -\lambda_1), \lambda_3 = \dots = \lambda_7 = 0$ , where

$$(2.9) \quad \lambda_1 = \left\{ \frac{m-1}{2 \sin^2 \chi} \left( \frac{e_1^2}{g_1^2} - \frac{2e_1 e_2}{g_1 g_2} \cos \chi + \frac{e_2^2}{g_2^2} \right) \right\}^{1/2}.$$

It is also to be noted that there are only four independent eigenvectors for the eigenvalue zero, see [3, 4] for more details. From (2.9) we see that  $\lambda_1$  is real for  $m > 1$  and purely imaginary for  $m < 1$ . The goal of this paper is to consider the case  $m > 1$ .

### 3. NUMERICAL APPROXIMATION

In this section we proceed to the numerical approximation of the conservation laws of 3-D WNLRT to study the evolution of a weakly nonlinear wavefront  $\Omega_t$  in three space dimensions and the formation and propagation of curves of singularities on it. Note that the system of conservation laws (2.2)-(2.3) and (2.7) can be recast in the usual divergence form

$$(3.1) \quad W_t + F_1(W)_{\xi_1} + F_2(W)_{\xi_2} = 0,$$

where the vector of conserved variables  $W$  and the flux-vectors  $F_1(W)$  and  $F_2(W)$  in the  $\xi_1$ - and  $\xi_2$ -directions respectively, are given by

$$(3.2) \quad \begin{aligned} W &= \left( g_1 \mathbf{u}, g_2 \mathbf{v}, (m-1)^2 e^{2(m-1)} g_1 g_2 \sin \chi \right)^T, \\ F_1(W) &= (m\mathbf{n}, \mathbf{0}, 0)^T, \\ F_2(W) &= (\mathbf{0}, m\mathbf{n}, 0)^T. \end{aligned}$$

**3.1. Semi-discrete Central Scheme.** In order to numerically solve (3.1), we first discretise the given domain. In our computations we use a rectangular grid with mesh sizes  $h_1$  and  $h_2$  respectively in  $\xi_1$ - and  $\xi_2$ -directions. We will denote by  $C_{i,j}$ , the cell centred around the point  $(\xi_{1i}, \xi_{2j})$ , i.e.  $C_{i,j} = [\xi_{1i} - h_1/2, \xi_{1i} + h_1/2] \times [\xi_{2j} - h_2/2, \xi_{2j} + h_2/2]$ . Let  $\Delta t$  be the time step and denote by  $\overline{W}_{i,j}$ , the cell average of  $W$  at time  $t$  taken over  $C_{i,j}$ , i.e.

$$(3.3) \quad \overline{W}_{i,j}(t) := \frac{1}{h_1 h_2} \int_{C_{i,j}} W(\xi_1, \xi_2, t) d\xi_1 d\xi_2.$$

From the given the cell averages  $\overline{W}_{i,j}^n$  at time  $t^n = n\Delta t$ , a piecewise linear interpolant is reconstructed, resulting in

$$(3.4) \quad W(\xi_1, \xi_2, t^n) = \sum_{i,j} \left( \overline{W}_{i,j}^n + W'_{i,j}(\xi_1 - \xi_{1i}) + W''_{i,j}(\xi_2 - \xi_{2j}) \right) \mathbb{1}_{i,j}(\xi_1, \xi_2),$$

where  $\mathbb{1}_{i,j}$  is the characteristic function of the cell  $C_{i,j}$  and  $W'_{i,j}$  and  $W^\wedge_{i,j}$  are respectively the discrete slopes in  $\xi_1$ - and  $\xi_2$ -directions. A possible computation of these slopes which results in an overall non-oscillatory scheme is given by a smooth central weighted essentially non-oscillatory (CWENO) limiter [19]

$$(3.5) \quad \begin{aligned} W'_{i,j} &= \text{CWENO} \left( \frac{\overline{W}_{i+1,j}^n - \overline{W}_{i,j}^n}{h_1}, \frac{\overline{W}_{i,j}^n - \overline{W}_{i-1,j}^n}{h_1} \right), \\ W^\wedge_{i,j} &= \text{CWENO} \left( \frac{\overline{W}_{i,j+1}^n - \overline{W}_{i,j}^n}{h_2}, \frac{\overline{W}_{i,j}^n - \overline{W}_{i,j-1}^n}{h_2} \right), \end{aligned}$$

where the CWENO function is defined by

$$(3.6) \quad \text{CWENO}(a, b) = \frac{\omega(a) \cdot a + \omega(b) \cdot b}{\omega(a) + \omega(b)}, \quad \omega(a) = (\epsilon + a^2)^{-2}, \quad \epsilon = 10^{-6}.$$

Using the reconstruction (3.4) we compute the extrapolated values on the boundary

$$(3.7) \quad \begin{aligned} W_{i,j}^{L(R)} &= \overline{W}_{i,j}^n \mp \frac{h_1}{2} W'_{i,j}, \quad W_{i,j}^{B(T)} = \overline{W}_{i,j}^n \mp \frac{h_2}{2} W^\wedge_{i,j}, \\ W_{i,j}^{LT(RT)} &= \overline{W}_{i,j}^n \mp \frac{h_1}{2} W'_{i,j} + \frac{h_2}{2} W^\wedge_{i,j}, \quad W_{i,j}^{LB(RB)} = \overline{W}_{i,j}^n \mp \frac{h_1}{2} W'_{i,j} - \frac{h_2}{2} W^\wedge_{i,j}. \end{aligned}$$

The starting point for the construction of the numerical scheme is a semi-discrete discretisation of (3.1). An integration of the balance law (3.1) over the cell  $C_{i,j}$  yields

$$(3.8) \quad \frac{d\overline{W}_{i,j}}{dt} = - \frac{\mathcal{F}_{1_{i+\frac{1}{2},j}} - \mathcal{F}_{1_{i-\frac{1}{2},j}}}{h_1} - \frac{\mathcal{F}_{2_{i,j+\frac{1}{2}}} - \mathcal{F}_{2_{i,j-\frac{1}{2}}}}{h_2}.$$

where the quantities  $\mathcal{F}_{i+1/2,j}$  and  $\mathcal{F}_{i,j+1/2}$  are respectively the numerical fluxes at the cell interfaces  $i + 1/2, j$  and  $i, j + 1/2$ . In a Riemann solver based upwind scheme, these fluxes are obtained by solving local Riemann problems. The central type schemes we employ here completely avoid the solving of Riemann problems.

In [22], Kurganov and Tadmor first derive a fully discrete central scheme by constructing an intermediate mesh of variable cell length, making use of the local speeds  $a_{i+1/2,j}, a_{i,j+1/2}$  of propagation at the cell interfaces, defined by

$$(3.9) \quad \begin{aligned} a_{i+\frac{1}{2},j} &:= \max \left\{ \rho \left( \frac{\partial F_1}{\partial W} (W_{i,j}^R) \right), \rho \left( \frac{\partial F_1}{\partial W} (W_{i+1,j}^L) \right) \right\}, \\ a_{i,j+\frac{1}{2}} &:= \max \left\{ \rho \left( \frac{\partial F_2}{\partial W} (W_{i,j}^T) \right), \rho \left( \frac{\partial F_2}{\partial W} (W_{i,j+1}^B) \right) \right\}. \end{aligned}$$

where  $\rho(A) = \max_i |\lambda_i(A)|$ ,  $\lambda_i(A)$  being the eigenvalues of the Jacobian matrix  $A$ . By letting the time-step tends to zero, i.e.  $\Delta t \rightarrow 0$ , the fully discrete scheme yields the semi-discrete formulation (3.8) which is very simple and robust, see [22] for the derivation. The numerical flux functions  $\mathcal{F}_{i+1/2,j}$  and  $\mathcal{F}_{i,j+1/2}$  in (3.8) can be obtained as

$$(3.10) \quad \begin{aligned} \mathcal{F}_{i+\frac{1}{2},j} (W_{i,j}^R, W_{i+1,j}^L) &= \frac{1}{2} (F_1 (W_{i+1,j}^L) + F_1 (W_{i,j}^R)) - \frac{a_{i+\frac{1}{2},j}}{2} (W_{i+1,j}^L - W_{i,j}^R), \\ \mathcal{F}_{i,j+\frac{1}{2}} (W_{i,j}^T, W_{i,j+1}^B) &= \frac{1}{2} (F_2 (W_{i,j+1}^B) + F_2 (W_{i,j}^T)) - \frac{a_{i,j+\frac{1}{2}}}{2} (W_{i,j+1}^B - W_{i,j}^T). \end{aligned}$$

Note that the numerical fluxes  $\mathcal{F}_{i+1/2,j}$  and  $\mathcal{F}_{i,j+1/2}$  depends only on the local speeds of propagation  $a_{i+1/2,j}$  and  $a_{i,j+1/2}$  and, due to its simple and general form, it can be implemented and extended to any spatial order straightforwardly.

To improve the temporal accuracy and to gain second order accuracy in time we use a TVD Runge-Kutta scheme [36] to numerically integrate the system of ODEs in (3.8). Denoting the right hand side of (3.8) by  $\mathcal{L}_{i,j}(W)$ , the second order Runge-Kutta scheme updates  $W$  through the following two stages

$$(3.11) \quad \begin{aligned} W_{i,j}^{(1)} &= \bar{W}_{i,j}^n + \Delta t \mathcal{L}_{i,j}(\bar{W}^n), \\ \bar{W}_{i,j}^{n+1} &= \frac{1}{2} \bar{W}_{i,j}^n + \frac{1}{2} W_{i,j}^{(1)} + \frac{1}{2} \Delta t \mathcal{L}_{i,j}(W^{(1)}). \end{aligned}$$

**3.2. Constrained Transport.** The geometric solenoidal constraint (2.6) of 3-D KCL needs special attention, because if it is not fulfilled exactly, it can produce non-physical solutions. Especially near the discontinuities, the error due to numerical discretisation can produce very large divergences of  $\mathfrak{B}_k$ . To avoid this, three additional transport equations have been introduced to the central scheme, by means of which the geometric solenoidal constraint can be enforced. This additional equations are relations for three potential functions  $\mathbb{A}_k$ ,  $k = 1, 2, 3$  which can be derived as follows.

We convert the six evolution equations (2.2)-(2.3) of the 3-D KCL system into three equations for the potentials  $\mathbb{A}_k$ . The existence of the potentials  $\mathbb{A}_k$  follow from the fact that the divergence of  $\mathfrak{B}_k$  is equal to zero, i.e.

$$(3.12) \quad \operatorname{div}(\mathfrak{B}_k) \equiv (g_2 v_k)_{\xi_1} + (-g_1 u_k)_{\xi_2} = 0.$$

Therefore, it follows that

$$(3.13) \quad \begin{aligned} g_1 u_k &= \mathbb{A}_{k\xi_1}, \\ g_2 v_k &= \mathbb{A}_{k\xi_2}. \end{aligned}$$

In the light of (3.13), the 3-D KCL system (2.2)-(2.3) reads

$$(3.14) \quad \begin{aligned} \mathbb{A}_{k\xi_1 t} - (mn_k)_{\xi_1} &= 0, \\ \mathbb{A}_{k\xi_2 t} - (mn_k)_{\xi_2} &= 0 \end{aligned}$$

and thus, we obtain

$$(3.15) \quad \mathbb{A}_{kt} - mn_k = 0.$$

From the definition (2.1) of the unit normal  $\mathbf{n}$  it follows that

$$(3.16) \quad \begin{aligned} \mathbf{n} &= \frac{g_1 \mathbf{u} \times g_2 \mathbf{v}}{\|g_1 \mathbf{u} \times g_2 \mathbf{v}\|} \\ &= \frac{\mathbb{A}_{\xi_1} \times \mathbb{A}_{\xi_2}}{\|\mathbb{A}_{\xi_1} \times \mathbb{A}_{\xi_2}\|}. \end{aligned}$$

Note that here we have denoted  $\mathbb{A} = (\mathbb{A}_1, \mathbb{A}_2, \mathbb{A}_3)$ . Hence, (3.15)-(3.16) yields the equations for  $\mathbb{A}_1, \mathbb{A}_2, \mathbb{A}_3$

$$(3.17) \quad \mathbb{A}_{1t} - m \frac{(\mathbb{A}_{2\xi_1} \mathbb{A}_{3\xi_2} - \mathbb{A}_{3\xi_1} \mathbb{A}_{2\xi_2})}{\sqrt{\mathbb{A}_{\xi_1}^2 \mathbb{A}_{\xi_2}^2 - (\mathbb{A}_{\xi_1} \cdot \mathbb{A}_{\xi_2})^2}} = 0,$$

$$(3.18) \quad \mathbb{A}_{2t} - m \frac{(\mathbb{A}_{3\xi_1} \mathbb{A}_{1\xi_2} - \mathbb{A}_{1\xi_1} \mathbb{A}_{3\xi_2})}{\sqrt{\mathbb{A}_{\xi_1}^2 \mathbb{A}_{\xi_2}^2 - (\mathbb{A}_{\xi_1} \cdot \mathbb{A}_{\xi_2})^2}} = 0,$$

$$(3.19) \quad \mathbb{A}_{3t} - m \frac{(\mathbb{A}_{1\xi_1} \mathbb{A}_{2\xi_2} - \mathbb{A}_{2\xi_1} \mathbb{A}_{1\xi_2})}{\sqrt{\mathbb{A}_{\xi_1}^2 \mathbb{A}_{\xi_2}^2 - (\mathbb{A}_{\xi_1} \cdot \mathbb{A}_{\xi_2})^2}} = 0.$$

Thus, (3.17)-(3.19) form the evolution equations for the three potential functions  $\mathbb{A}_1, \mathbb{A}_2, \mathbb{A}_3$ . It is interesting to note that (3.17)-(3.19) forms a coupled system of three fully nonlinear PDEs, each of them is of the Hamilton-Jacobi type. The basic idea behind the constrained transport is to make use of  $\mathbb{A}_1, \mathbb{A}_2, \mathbb{A}_3$  to get the values of  $g_1\mathbf{u}$  and  $g_2\mathbf{v}$ . These corrected values should fulfil a discrete version of the geometric solenoidal constraint.

In each time step the system of conservation laws (3.1) is approximated by the central scheme (3.8). Using the solution thus obtained we compute the updated values of  $\mathbb{A}_1, \mathbb{A}_2, \mathbb{A}_3$ . The corrected values of  $g_1\mathbf{u}$  and  $g_2\mathbf{v}$  are then obtained from (3.13). It is the discretisation of the derivatives in (3.13) enforces the geometric solenoidal constraint. The decisive point is how to approximate this derivatives. We follow the procedure described by Rossmannith [32]. He proposes to use a staggered grid and to arrange the variables on the grids as depicted in Figure 1.

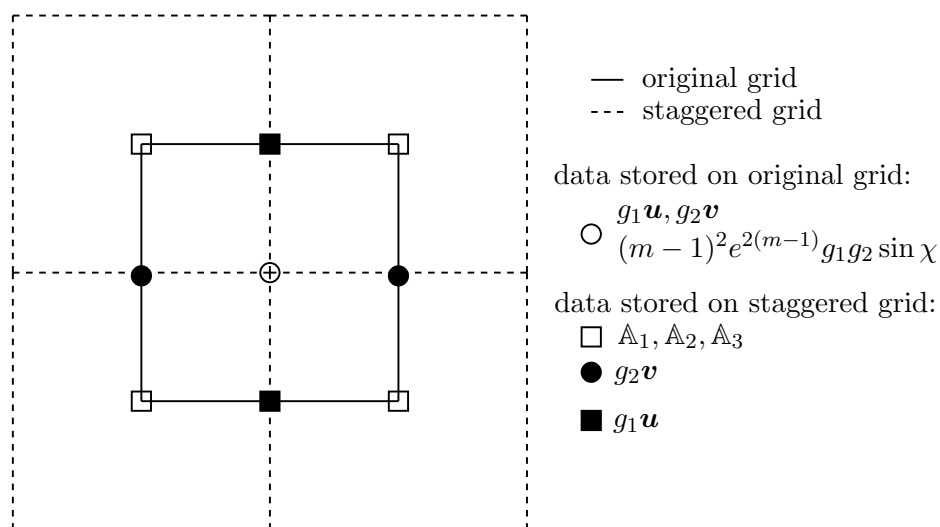


FIGURE 1. Arrangement of the variables on the grids.

- The potentials  $\mathbb{A}_1, \mathbb{A}_2, \mathbb{A}_3$  are computed at the midpoints of the staggered grid which coincide with the corners of the original grid.
- The vector  $g_1\mathbf{u}$  lies at the east and west edges of the staggered grid, which are the north and south edges of the original grid.
- The vector  $g_2\mathbf{v}$  lies at the north and south edges of the staggered grid, which are the east and west edges of the original grid.

With this arrangement, the derivatives of  $\mathbb{A}_1, \mathbb{A}_2, \mathbb{A}_3$  in the equation (3.13) can be approximated by central differences and the corrected values of the vectors  $g_1\mathbf{u}$  and  $g_2\mathbf{v}$  are obtained as

$$(3.20) \quad \begin{aligned} [g_1 u_k]_{i,j+\frac{1}{2}}^{n+1} &= \frac{1}{h_1} \left( \mathbb{A}_{k_{i+\frac{1}{2},j+\frac{1}{2}}}^{n+1} - \mathbb{A}_{k_{i-\frac{1}{2},j+\frac{1}{2}}}^{n+1} \right), \\ [g_2 v_k]_{i+\frac{1}{2},j}^{n+1} &= \frac{1}{h_2} \left( \mathbb{A}_{k_{i+\frac{1}{2},j+\frac{1}{2}}}^{n+1} - \mathbb{A}_{k_{i+\frac{1}{2},j-\frac{1}{2}}}^{n+1} \right). \end{aligned}$$

We now consider a cell of the original grid. The corrected values of  $g_1\mathbf{u}$  and  $g_2\mathbf{v}$  lie on the edges of that cell. In the discrete formula for the geometric solenoidal constraint (2.6), the derivatives are

approximated by central differences of  $g_1\mathbf{u}$  and  $g_2\mathbf{v}$  values on the edges to get

$$(3.21) \quad [\operatorname{div}(\mathfrak{B}_k)]_{i,j}^{n+1} = \frac{[g_2v_k]_{i+\frac{1}{2},j}^{n+1} - [g_2v_k]_{i-\frac{1}{2},j}^{n+1}}{h_1} - \frac{[g_1u_k]_{i,j+\frac{1}{2}}^{n+1} - [g_1u_k]_{i,j-\frac{1}{2}}^{n+1}}{h_2}.$$

Replacing the values of  $g_1u_k$  and  $g_2v_k$  on the cell edges by the expressions in (3.20), it can be seen that the right hand side of (3.21) vanishes. Thus, we have devised a method to get the corrected values of  $g_1\mathbf{u}$  and  $g_2\mathbf{v}$  so that a discrete version of the geometric solenoidal constraint is satisfied.

It remains to be discussed how to get the updated values of  $\mathbb{A}_1, \mathbb{A}_2, \mathbb{A}_3$ . There are several different approaches for the constrained transport in the MHD literature, see [5, 13, 32, 33] and the references therein. As it can be seen from (3.17)-(3.19), the evolution equations for  $\mathbb{A}_1, \mathbb{A}_2, \mathbb{A}_3$  form a coupled system of nonlinear equations. Hence, directly discretising them could be tedious and time consuming. The decisive step is to use instead, the equation (3.15) to get the staggered update for  $\mathbb{A}_1, \mathbb{A}_2, \mathbb{A}_3$ . Integrating and averaging (3.15) over a staggered grid yields the semi-discrete approximation

$$(3.22) \quad \frac{d}{dt} [\mathbb{A}_k]_{i+\frac{1}{2},j+\frac{1}{2}} = [mn_k]_{i+\frac{1}{2},j+\frac{1}{2}}.$$

The above equation (3.22) can be used to get the updated values of the staggered averages of the potentials  $\mathbb{A}_1, \mathbb{A}_2, \mathbb{A}_3$ . However, in order to use (3.22) we need to have the values of  $mn_k$  at the corners of the grid cells. At this point, we note that  $mn_k$  is precisely the nonzero element in the flux functions  $F_1$  and  $F_2$  of the system (3.1) of conservation laws of 3-D WNLRT. Since the numerical flux functions  $\mathcal{F}_1$  and  $\mathcal{F}_2$  at the interfaces are already available from the central scheme, following the approach of Ryu et al. [33] we take

$$(3.23) \quad [mn_k]_{i+\frac{1}{2},j+\frac{1}{2}} = \frac{1}{4} \left( [mn_k]_{i+\frac{1}{2},j} + [mn_k]_{i+\frac{1}{2},j+1} + [mn_k]_{i,j+\frac{1}{2}} + [mn_k]_{i+1,j+\frac{1}{2}} \right).$$

Using (3.23) in (3.22) and discretising the resulting system of ODEs using the same Runge-Kutta method (3.11) gives the staggered updates for  $\mathbb{A}_1, \mathbb{A}_2, \mathbb{A}_3$ .

Thus, we have devised a way to compute the values of  $g_1\mathbf{u}$  and  $g_2\mathbf{v}$  so that the discrete divergence of the three vectors  $\mathfrak{B}_k$  equals zero. An algorithm, in which the solution of the 3-D WNLRT equations calculated using the central scheme (3.8) is corrected accordingly in each time step, can be written in the following form.

- (1) The system of conservation laws (3.1) is solved using the central scheme, giving the values of the conserved variable  $W$ . The vectors  $\mathfrak{B}_k$  are not yet divergence free, it will be corrected in the next steps.
- (2) The potentials  $\mathbb{A}_1, \mathbb{A}_2, \mathbb{A}_3$  are updated by solving (3.22).
- (3) The spatial derivatives of  $\mathbb{A}_1, \mathbb{A}_2, \mathbb{A}_3$  are calculated and the corrected values of  $g_1\mathbf{u}$  and  $g_2\mathbf{v}$  are obtained using (3.20).
- (4) The values of  $g_1\mathbf{u}$  and  $g_2\mathbf{v}$  on the cell edges are averaged, to get the values at the cell centres of the original grid

$$(3.24) \quad \begin{aligned} [g_1\mathbf{u}]_{i,j}^{n+1} &= \frac{1}{2} \left( [g_1\mathbf{u}]_{i,j-\frac{1}{2}}^{n+1} + [g_1\mathbf{u}]_{i,j+\frac{1}{2}}^{n+1} \right), \\ [g_2\mathbf{v}]_{i,j}^{n+1} &= \frac{1}{2} \left( [g_2\mathbf{v}]_{i-\frac{1}{2},j}^{n+1} + [g_2\mathbf{v}]_{i+\frac{1}{2},j}^{n+1} \right). \end{aligned}$$

**3.3. Formulation of Initial and Boundary Conditions.** To complete the algorithm, the initialisation of the data on the respective grids and the implementation of appropriate boundary conditions are to be done. The initial data for the system (3.1) can be formulated as follows.

Let the initial position of a weakly nonlinear wavefront  $\Omega_t$  be given a parametric form

$$(3.25) \quad \Omega_0: \mathbf{x} = \mathbf{x}_0(\xi_1, \xi_2).$$

Given the representation (3.25), the initial values of the metrics  $g_1$  and  $g_2$  and the unit tangent vectors  $\mathbf{u}$  and  $\mathbf{v}$  can be taken as

$$(3.26) \quad g_{10} = \|\mathbf{x}_{0\xi_1}\|, \quad g_{20} = \|\mathbf{x}_{0\xi_2}\|,$$

$$(3.27) \quad \mathbf{u}_0 = \frac{\mathbf{x}_{0\xi_1}}{\|\mathbf{x}_{0\xi_1}\|}, \quad \mathbf{v}_0 = \frac{\mathbf{x}_{0\xi_2}}{\|\mathbf{x}_{0\xi_2}\|}.$$

Note that

$$(3.28) \quad (g_{20}\mathbf{v}_0)_{\xi_1} - (g_{10}\mathbf{u}_0)_{\xi_2} = \mathbf{x}_{0\xi_2\xi_1} - \mathbf{x}_{0\xi_1\xi_2} = 0.$$

Therefore, we see that the geometric solenoidal constraint (2.6) is satisfied by the initial values of  $g_1\mathbf{u}$  and  $g_2\mathbf{v}$ . The unit normal  $\mathbf{n}_0$  of  $\Omega_0$  is given by

$$(3.29) \quad \mathbf{n}_0 = \frac{\mathbf{u}_0 \times \mathbf{v}_0}{\|\mathbf{u}_0 \times \mathbf{v}_0\|}$$

so that the three vectors  $(\mathbf{u}_0, \mathbf{v}_0, \mathbf{n}_0)$  forms a right handed system. Let the distribution of the front velocity be given by

$$(3.30) \quad m = m_0(\xi_1, \xi_2).$$

Given the initial values of  $g_1, g_2, \mathbf{u}, \mathbf{v}$  and  $m$ , the initial value of the conserved variable  $W$  can be easily calculated. The potentials  $\mathbb{A}_1, \mathbb{A}_2, \mathbb{A}_3$  need to be initialised on the staggered grids. Here care has to be taken, because the relation (3.13) has to be fulfilled. It is easy to check that the choice

$$(3.31) \quad \begin{aligned} \mathbb{A}_{10}(\xi_1, \xi_2) &= x_{01}(\xi_1, \xi_2), \\ \mathbb{A}_{20}(\xi_1, \xi_2) &= x_{02}(\xi_1, \xi_2), \\ \mathbb{A}_{30}(\xi_1, \xi_2) &= x_{03}(\xi_1, \xi_2). \end{aligned}$$

will serve the purpose. Hence, formulation of the initial data is completed.

We now proceed to the discussion of the boundary conditions. Firstly, we note that the data in the boundary cells of the staggered cells needs special attention. The staggered grid at each side is half a cell larger than the original grid. Therefore, some sort of boundary condition has to be implemented in order to be able to calculate the data in the boundary cells of the staggered grid.

There are two ways of proceeding. In the first method, a ghost cell layer boundary boundary condition for the potentials  $\mathbb{A}_k$  could be implemented. In this case, the values of  $g_1\mathbf{u}$  and  $g_2\mathbf{v}$  are calculated according to (3.13) in all points where they are needed. This has the advantage that the discrete geometric solenoidal constraint is satisfied at the boundary cells too. However, when a ghost cell layer boundary condition is implemented, the values in the boundary cells are the copies of the values in the neighbouring cells. As a result, the spatial derivatives of  $\mathbb{A}_k$  in (3.13) vanishes at the boundary cells. This in turn lead to zero values for  $g_1\mathbf{u}$  and  $g_2\mathbf{v}$  at the boundary, independently of their physically exact values. This can produce oscillations in the solution.

We can alternatively implement a boundary condition for the variables  $g_1\mathbf{u}$  and  $g_2\mathbf{v}$ . This can be done by a ghost cell boundary condition or a periodic boundary condition depending on the problem. In this case the potentials  $\mathbb{A}_k$  need not be calculated in the boundary cells. Moreover, the boundary values of  $g_1\mathbf{u}$  and  $g_2\mathbf{v}$  will be much more conform with those that are physically correct. Only now (3.13) is no longer used and the discrete geometric solenoidal constraint is not enforced at the boundary. However, the constraint is satisfied in the interior cells and there are no oscillations in the solution if this alternative is chosen.

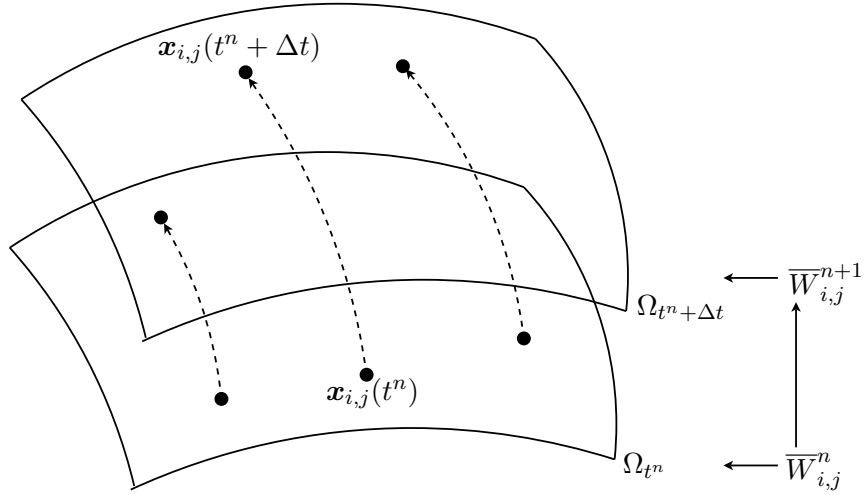


FIGURE 2. Geometrical representation of the time marching scheme. The dotted lines denote the rays.

**3.4. Method of Construction of Successive Fronts.** We now proceed to explain the method of calculation of the successive positions of the nonlinear wavefront  $\Omega_t$ . At any time  $t$ , given the values of  $g_1, g_2, \mathbf{u}, \mathbf{v}$  and  $m$ , we first compute the value of the conserved variable  $W$ . Using these values we numerically solve the system (3.1) to get the updated value of  $W$  at time  $t + \Delta t$ . Since  $\|\mathbf{u}\| = \|\mathbf{v}\| = 1$ , from the first six components of  $W$  the values of  $g_1, g_2, \mathbf{u}$  and  $\mathbf{v}$  can be computed very easily. The unit normal  $\mathbf{n}$  is then given by (2.1). To get the updated value of the normal velocity  $m$  we proceed as follows. Notice that, say,

$$(3.32) \quad (m-1)^2 e^{2(m-1)} = \frac{W_7}{g_1 g_2 \sin \chi} \equiv \kappa.$$

We now solve the nonlinear equation

$$(3.33) \quad \vartheta(m) \equiv (m-1)^2 e^{2(m-1)} - \kappa = 0$$

for  $m$  using Newton-Raphson method. The monotonicity of the function  $\vartheta$  in  $(1, \infty)$  ensures the uniqueness of the solution of (3.33).

At any time  $t$ , we approximate the front  $\Omega_t$  by a discrete set of points  $\mathbf{x}_{i,j}(t)$ , where

$$(3.34) \quad \mathbf{x}_{i,j}(t) := \mathbf{x}(\xi_{1i}, \xi_{2j}, t).$$

To get the successive positions of  $\Omega_t$ , we numerically solve the system of ODEs

$$(3.35) \quad \frac{d\mathbf{x}_{i,j}(t)}{dt} = m_{i,j}(t) \mathbf{n}_{i,j}(t),$$

where  $m_{i,j}(t)$  and  $\mathbf{n}_{i,j}(t)$  are the corresponding values of  $m$  and  $\mathbf{n}$  obtained from  $\overline{W}_{i,j}(t)$ . A pictorial representation of our time-marching scheme is depicted in Figure 2. For the numerical integration of the system of ODEs in (3.35), we have employed the same TVD Runge-Kutta time stepping

scheme given in (3.11). Using this procedure, we obtain the updated values of  $(x_1, x_2, x_3)$  and this gives the successive positions of the front  $\Omega_t$ .

#### 4. ANALYSIS OF LINEARISED CAUCHY PROBLEM

It is well known from the literature [15, 20, 21, 24, 40] that weakly hyperbolic systems give rise to a Jordan mode. The solution to a Cauchy problem for such a system typically contains a mode which grows linearly in time. This component, the so called Jordan mode is in the direction of the corresponding generalised eigenvector. However, the numerical solution of the 3-D WNLRT system does not exhibit any such component. The reason for the disappearance of this mode is the geometric solenoidal constraint (2.6), which is inherent to the system of equations. Due to the nonlinearity and complexity of the equations, we are unable to prove this result for the full nonlinear system. Nonetheless, to support our assertion, we prove the result for the linearised 3-D WNLRT system. We strongly believe the same result to hold also for the full nonlinear system.

For convenience in this section<sup>1</sup> we denote  $\mathbf{U} = g_1 \mathbf{u}$ ,  $\mathbf{V} = g_2 \mathbf{v}$ . The 3-D WNLRT system (2.2)-(2.3) and (2.7) with this new notation reads

$$\begin{aligned} (4.1) \quad & \mathbf{U}_t - (m\mathbf{n})_{\xi_1} = 0, \\ (4.2) \quad & \mathbf{V}_t - (m\mathbf{n})_{\xi_2} = 0, \\ (4.3) \quad & \left( (m-1)^2 e^{2(m-1)} \|\mathbf{U} \times \mathbf{V}\| \right)_t = 0. \end{aligned}$$

Let us consider a planar wavefront given by

$$(4.4) \quad \Omega_t: x_1 = \xi_1, \quad x_2 = \xi_2, \quad x_3 = m_0 t.$$

where we assume  $m_0 > 1$ . The unknown variables  $\mathbf{U}$ ,  $\mathbf{V}$  and  $m$  assume constant values on  $\Omega_t$  and they can be easily obtained to be

$$(4.5) \quad \tilde{\mathbf{U}} = (1, 0, 0), \quad \tilde{\mathbf{V}} = (0, 1, 0), \quad \tilde{m} = m_0.$$

We linearise the 3-D WNLRT system (4.1)-(4.3) about this constant state (4.5). After simplifications the linearised equations read

$$(4.6) \quad \begin{pmatrix} U_1 \\ U_2 \\ U_3 \\ V_1 \\ V_2 \\ V_3 \\ m \end{pmatrix}_t + \begin{pmatrix} m_0 U_3 \\ m_0 V_3 \\ -m \\ 0 \\ 0 \\ 0 \\ -\frac{(m_0-1)}{2} U_3 \end{pmatrix}_{\xi_1} + \begin{pmatrix} 0 \\ 0 \\ 0 \\ m_0 U_3 \\ m_0 V_3 \\ -m \\ -\frac{(m_0-1)}{2} V_3 \end{pmatrix}_{\xi_2} = 0.$$

Let  $W = (U_1, U_2, U_3, V_1, V_2, V_3, m)^T$ . The linearised system (4.6) can then be recast in the usual matrix form

$$(4.7) \quad W_t + A_1 W_{\xi_1} + A_2 W_{\xi_2} = 0,$$

---

<sup>1</sup>These notations are used only in this section.

where

$$(4.8) \quad A_1 = \begin{pmatrix} 0 & 0 & m_0 & 0 & 0 & 0 & 0 \\ 0 & 0 & 0 & 0 & 0 & m_0 & 0 \\ 0 & 0 & 0 & 0 & 0 & 0 & -1 \\ 0 & 0 & 0 & 0 & 0 & 0 & 0 \\ 0 & 0 & 0 & 0 & 0 & 0 & 0 \\ 0 & 0 & 0 & 0 & 0 & 0 & 0 \\ 0 & 0 & -\frac{(m_0-1)}{2} & 0 & 0 & 0 & 0 \end{pmatrix}, \quad A_2 = \begin{pmatrix} 0 & 0 & 0 & 0 & 0 & 0 & 0 \\ 0 & 0 & 0 & 0 & 0 & 0 & 0 \\ 0 & 0 & 0 & 0 & 0 & 0 & 0 \\ 0 & 0 & m_0 & 0 & 0 & 0 & 0 \\ 0 & 0 & 0 & 0 & 0 & m_0 & 0 \\ 0 & 0 & 0 & 0 & 0 & 0 & -1 \\ 0 & 0 & 0 & 0 & 0 & -\frac{(m_0-1)}{2} & 0 \end{pmatrix}.$$

Consider  $(\nu_1, \nu_2) \in \mathbb{R}^2$  with  $\nu_1^2 + \nu_2^2 = 1$ . The matrix pencil  $A = \nu_1 A_1 + \nu_2 A_2$  has the eigenvalues

$$(4.9) \quad \lambda_1 = \sqrt{\frac{m_0-1}{2}}, \lambda_2 = -\lambda_1, \lambda_3 = \dots = \lambda_7 = 0.$$

We note that like the original system (4.1)-(4.3), the linearised system (4.6) is also degenerate as the eigenvalue zero has multiplicity five but the associated eigenspace is only four-dimensional. We now proceed to solve a Cauchy problem for (4.6). Let an initial data for (4.6) be given by

$$(4.10) \quad W(\xi_1, \xi_2, 0) = W_0(\xi_1, \xi_2).$$

**Theorem 4.1.** *The solution to the Cauchy problem (4.7) and (4.10) does not contain any linearly growing Jordan mode when the constraint*

$$(4.11) \quad V_{3\xi_1} - U_{3\xi_2} = 0$$

is satisfied at  $t = 0$ .

*Proof.* The solution of the Cauchy problem (4.6) and (4.10) can be obtained using the Fourier transform method. The Fourier transform of  $W$  with respect to the space variables  $\xi_1, \xi_2$  is defined via

$$(4.12) \quad \widehat{W}(k_1, k_2, t) := \int_{-\infty}^{\infty} \int_{-\infty}^{\infty} W(\xi_1, \xi_2, t) e^{-i(k_1 \xi_1 + k_2 \xi_2)} d\xi_1 d\xi_2.$$

Taking the Fourier transform of (4.7) yields

$$(4.13) \quad \widehat{W}_t + i(k_1 A_1 + k_2 A_2) \widehat{W} = 0.$$

The initial data for (4.13) is obtained by taking Fourier transform of (4.10)

$$(4.14) \quad \widehat{W}(k_1, k_2, 0) = \widehat{W}_0(k_1, k_2).$$

The solution of the Cauchy problem (4.13)-(4.14) is given by

$$(4.15) \quad \widehat{W}(k_1, k_2, t) = e^{-it(k_1 A_1 + k_2 A_2)} \widehat{W}_0(k_1, k_2).$$

Let  $k = \sqrt{k_1^2 + k_2^2}$  so that  $(k_1, k_2) = k(\nu_1, \nu_2)$  with  $\nu_1^2 + \nu_2^2 = 1$ . Reducing the matrix pencil  $A$  to Jordan canonical form yields

$$(4.16) \quad J = \begin{pmatrix} 0 & 1 & 0 & 0 & 0 & 0 & 0 \\ 0 & 0 & 0 & 0 & 0 & 0 & 0 \\ 0 & 0 & c & 0 & 0 & 0 & 0 \\ 0 & 0 & 0 & -c & 0 & 0 & 0 \\ 0 & 0 & 0 & 0 & 0 & 0 & 0 \\ 0 & 0 & 0 & 0 & 0 & 0 & 0 \\ 0 & 0 & 0 & 0 & 0 & 0 & 0 \end{pmatrix},$$

where  $c := \sqrt{(m_0 - 1)/2}$ . Let  $P$  be a non-singular matrix of right eigenvectors of  $A$  including a generalised eigenvector. We note that  $P$  satisfies

$$(4.17) \quad AP = PJ.$$

Using the Jordan matrix (4.16) the columns of  $P$  can be obtained by solving the eigenvalue problems

$$(4.18) \quad Ap_1 = 0, \quad Ap_2 = p_1, \quad Ap_3 = cp_3, \quad Ap_4 = -cp_4, \quad Ap_5 = Ap_6 = Ap_7 = 0.$$

Notice that  $p_2$  is the generalised eigenvector. After algebraic computations we obtain the transformation matrix

$$(4.19) \quad P = \begin{pmatrix} -\nu_1\nu_2m_0 & 0 & -\frac{2\nu_1^2m_0}{m_0-1} & -\frac{2\nu_1^2m_0}{m_0-1} & 1 & 0 & 0 \\ \nu_1^2m_0 & 0 & -\frac{2\nu_1\nu_22m_0}{m_0-1} & -\frac{2\nu_1\nu_22m_0}{m_0-1} & 0 & 1 & 0 \\ 0 & -\nu_2 & \sqrt{\frac{2}{m_0-1}}\nu_1 & -\sqrt{\frac{2}{m_0-1}}\nu_1 & 0 & 0 & 0 \\ -\nu_2^2m_0 & 0 & -\frac{2\nu_1\nu_22m_0}{m_0-1} & -\frac{2\nu_1\nu_22m_0}{m_0-1} & 0 & 0 & 1 \\ \nu_1\nu_2m_0 & 0 & -\frac{2\nu_2^2m_0}{m_0-1} & -\frac{2\nu_2^2m_0}{m_0-1} & 0 & 0 & 0 \\ 0 & \nu_1 & \sqrt{\frac{2}{m_0-1}}\nu_2 & -\sqrt{\frac{2}{m_0-1}}\nu_2 & 0 & 0 & 0 \\ 0 & 0 & 1 & 1 & 0 & 0 & 0 \end{pmatrix}.$$

The matrix exponential in the equation (4.15) can be computed as

$$(4.20) \quad Pe^{-iktJ}P^{-1} = \begin{pmatrix} 1 & 0 & \frac{m_0tk_1k_2^2}{k^3} & 0 & 0 & -\frac{m_0tk_1^2k_2}{k^3} & \frac{2m_0}{m_0-1} \frac{k_1^2(1-\cos(ktc))}{k^2} \\ 0 & 1 & -\frac{m_0tk_1^2k_2}{k^3} & 0 & 0 & \frac{m_0tk_1^3}{k^3} & \frac{2m_0}{m_0-1} \frac{k_1k_2(1-\cos(ktc))}{k^2} \\ 0 & 0 & \frac{k_1^2\cos(ktc)+k_2^2}{k^2} & 0 & 0 & -\frac{k_1k_2(1-\cos(ktc))}{k^2} & 0 \\ 0 & 0 & \frac{m_0tk_2^3}{k^3} & 1 & 0 & -\frac{m_0tk_1k_2^2}{k^3} & \frac{2m_0}{m_0-1} \frac{k_1^2(1-\cos(ktc))}{k^2} \\ 0 & 0 & -\frac{m_0tk_1k_2^2}{k^3} & 0 & 1 & \frac{m_0tk_1^2k_2}{k^3} & \frac{2m_0}{m_0-1} \frac{k_2^2(1-\cos(ktc))}{k^2} \\ 0 & 0 & -\frac{k_1k_2(1-\cos(ktc))}{k^2} & 0 & 0 & \frac{k_1^2+k_2^2\cos(ktc)}{k^2} & 0 \\ 0 & 0 & 0 & 0 & 0 & 0 & \cos(ktc) \end{pmatrix}$$

Using (4.20) in (4.15) we obtain the final solution

$$(4.21) \quad \begin{aligned} \widehat{U}_1(k_1, k_2, t) = & \widehat{U}_{10}(k_1, k_2) - m_0 t \frac{k_1 k_2}{k^3} \left( k_1 \widehat{V}_{30} - k_2 \widehat{U}_{30} \right) (k_1, k_2) \\ & + \frac{2m_0}{m_0 - 1} \frac{k_1^2 (1 - \cos(ktc))}{k^2} \widehat{m}_0(k_1, k_2), \end{aligned}$$

$$(4.22) \quad \begin{aligned} \widehat{U}_2(k_1, k_2, t) = & \widehat{U}_{20}(k_1, k_2) + m_0 t \frac{k_1^2}{k^3} \left( k_1 \widehat{V}_{30} - k_2 \widehat{U}_{30} \right) (k_1, k_2) \\ & + \frac{2m_0}{m_0 - 1} \frac{k_1 k_2 (1 - \cos(ktc))}{k^2} \widehat{m}_0(k_1, k_2), \end{aligned}$$

$$(4.23) \quad \widehat{U}_3(k_1, k_2, t) = \frac{1}{k^2} (k_1^2 \cos(ktc) + k_2^2) \widehat{U}_{30}(k_1, k_2) - \frac{k_1 k_2}{k^2} (1 - \cos(ktc)) \widehat{V}_{30}(k_1, k_2),$$

$$(4.24) \quad \begin{aligned} \widehat{V}_1(k_1, k_2, t) = & \widehat{V}_{10}(k_1, k_2) - m_0 t \frac{k_2^2}{k^3} \left( k_1 \widehat{V}_{30} - k_2 \widehat{U}_{30} \right) (k_1, k_2) \\ & + \frac{2m_0}{m_0 - 1} \frac{k_1 k_2 (1 - \cos(ktc))}{k^2} \widehat{m}_0(k_1, k_2), \end{aligned}$$

$$(4.25) \quad \begin{aligned} \widehat{V}_2(k_1, k_2, t) = & \widehat{U}_0(k_1, k_2) + m_0 t \frac{k_1 k_2}{k^3} \left( k_1 \widehat{V}_{30} - k_2 \widehat{U}_{30} \right) (k_1, k_2) \\ & + \frac{2m_0}{m_0 - 1} \frac{k_2^2 (1 - \cos(ktc))}{k^2} \widehat{m}_0(k_1, k_2), \end{aligned}$$

$$(4.26) \quad \widehat{V}_3(k_1, k_2, t) = -\frac{k_1 k_2}{k^2} (1 - \cos(ktc)) \widehat{U}_{30}(k_1, k_2) + \frac{1}{k^2} (k_1^2 + k_2^2 \cos(ktc)) \widehat{V}_{30}(k_1, k_2),$$

$$(4.27) \quad \widehat{m}(k_1, k_2, t) = \cos(ktc) \widehat{m}_0(k_1, k_2).$$

From the equations (4.21)-(4.27) we infer that the expressions for  $\widehat{U}_1, \widehat{U}_2, \widehat{V}_1$  and  $\widehat{V}_2$  contain a term with  $t$  multiplied by a factor  $k_1 \widehat{V}_{30} - k_2 \widehat{U}_{30}$ . It is very crucial that  $k_1 \widehat{V}_{30} - k_2 \widehat{U}_{30}$  is the Fourier transform of  $V_{30\xi_1} - U_{30\xi_2}$ . From the system (4.6) one can observe that the quantity  $V_{\xi_1} - U_{\xi_2}$  remains constant in time. Hence, when the constraint

$$(4.28) \quad V_{3\xi_1} - U_{3\xi_2} = 0 \text{ at } t = 0$$

is satisfied the term in (4.21)-(4.22) and (4.24)-(4.25), which grows linearly with  $t$  vanishes. The unknowns  $\mathbf{U}, \mathbf{V}$  and  $m$  are obtained by taking the inverse Fourier transform of (4.21)-(4.27) in which  $t$  appears only as a parameter. Definitely, the inversion will not introduce any additional term growing with  $t$ . Thus, we conclude that under the constraint (4.28) the Jordan mode in the solutions (4.21)-(4.27) disappears.  $\square$

*Remark 4.2.* It is worth noting that (4.28) is only one component of the vector constraint

$$(4.29) \quad \mathbf{V}_{\xi_1} - \mathbf{U}_{\xi_2} = 0 \text{ at } t = 0.$$

Had we taken the base state in (4.5) as  $\tilde{\mathbf{U}} = (0, 1, 0), \tilde{\mathbf{V}} = (0, 0, 1)$  (or  $\tilde{\mathbf{U}} = (0, 0, 1), \tilde{\mathbf{V}} = (1, 0, 0)$ ), then the condition (4.28) would have been replaced by  $V_{1\xi_1} - U_{1\xi_2} = 0$  at  $t = 0$  (or  $V_{2\xi_1} - U_{2\xi_2} = 0$  at  $t = 0$ ).

## 5. NUMERICAL CASE STUDIES

In order to illustrate the applicability of 3-D KCL for the modelling of evolution of nonlinear wavefronts, in this section we present a few illustrating examples. These examples reveal several

genuinely three-dimensional geometrical features of nonlinear wavefronts. In all the test problems considered, we have used the CFL condition

$$(5.1) \quad \Delta t \max \left( \frac{\rho_1}{h_1}, \frac{\rho_2}{h_2} \right) = \nu,$$

where  $\rho_1$  and  $\rho_2$  are respectively the maximum of the absolute values of the eigenvalues of the flux Jacobian matrices in  $\xi_1$ - and  $\xi_2$ -directions and  $\nu$  is the CFL number. In (5.1), the maximum is taken over all mesh cells. We have set  $\nu = 0.9$  in all our numerical experiments.

**5.1. Propagation of a Non-axisymmetric Nonlinear Wavefront.** We choose initial wavefront  $\Omega_0$  in a such a way that it is not axisymmetric. The front  $\Omega_0$  has a single smooth dip. The initial shape of the wavefront is given by

$$(5.2) \quad \Omega_0: x_3 = \frac{-\kappa}{1 + \frac{x_1^2}{\alpha^2} + \frac{x_2^2}{\beta^2}},$$

where the parameter values are set to be  $\kappa = 1/2, \alpha = 3/2, \beta = 3$ . The ray coordinates  $(\xi_1, \xi_2)$  are chosen initially as  $\xi_1 = x_1$  and  $\xi_2 = x_2$ . Therefore, using (5.2), the initial wavefront can be represented in a parametric form

$$(5.3) \quad x_1 = \xi_1, \quad x_2 = \xi_2, \quad x_3 = \frac{-\kappa}{1 + \frac{\xi_1^2}{\alpha^2} + \frac{\xi_2^2}{\beta^2}}.$$

With the aid of (5.3) the initial values  $g_1, g_2, \mathbf{u}$  and  $\mathbf{v}$  are calculated, cf. section 3.3. The normal velocity is prescribed as a constant  $m_0 = 1.2$  everywhere on the initial wavefront  $\Omega_0$ .

The computational domain  $[-20, 20] \times [-20, 20]$  is divided into  $401 \times 401$  mesh points. The simulations are done up to  $t = 2.0, 6.0, 10.0$ . We have set non-reflecting boundary conditions everywhere.

In Figure 3 we plot the initial wavefront  $\Omega_0$  and the successive positions of the wavefront  $\Omega_t$  at times  $t = 2.0, 6.0, 10.0$ . It can be seen that the wavefront has moved up in the  $x_3$ -direction and the dip has spread over a larger area in  $x_1$ - and  $x_2$ -directions. The lower part of the front moves up leading to a change in shape of the initial front  $\Omega_0$ . It is very interesting to note that two dips appear at the centre of the wavefront, which are clearly visible at  $t = 6.0$  and  $t = 10.0$ . These two dips are separated by an elevation almost like a wall parallel to the  $x_2$ -axis. There is a pair of kink lines, which are also parallel to the  $x_2$ -axis and are more clearly seen in Figure 4.

To explain the results of convergence of the rays we also give in Figure 4 the slices of the wavefront in  $x_2 = 0$  section and  $x_1 = 0$  section from time  $t = 0.0$  to  $t = 10.0$ . Due to the particular choice of the parameters  $\alpha$  and  $\beta$  in the initial data (5.2), the section of the front  $\Omega_0$  in  $x_2 = 0$  plane has a smaller radius of curvature than that of the section in  $x_1 = 0$  plane. This results in a stronger convergence of the rays in  $x_2 = 0$  plane compared to those in  $x_1 = 0$  plane as evident from Figure 4. In the diagram on the top in Figure 4, we clearly note a pair of kinks at times  $t = 3.0$  onwards in the  $x_2 = 0$  section. However, there are no kinks in the bottom diagram in Figure 4 in  $x_1 = 0$  section.

We give now the plots of the normal velocity  $m$  in  $(\xi_1, \xi_2)$  plane along  $\xi_1$ - and  $\xi_2$ -directions in Figure 5. It is observed that  $m$  has two shocks in the  $\xi_1$ -direction which correspond to the two kinks in the  $x_1$ -direction.

We plot the divergence of  $\mathfrak{B}_1$  at time  $t = 10.0$  computed using the formula (3.21) in Figure 6. It is evident that the geometric solenoidal condition is satisfied with an error of  $10^{-15}$ . The divergences of  $\mathfrak{B}_2$  and  $\mathfrak{B}_3$  also show the same trend.

The analysis of the linearised Cauchy problem for 3-D WNLRT in section 4 shows that when the geometric solenoidal constraint (2.6) is satisfied, the Jordan mode does not appear in the solution.

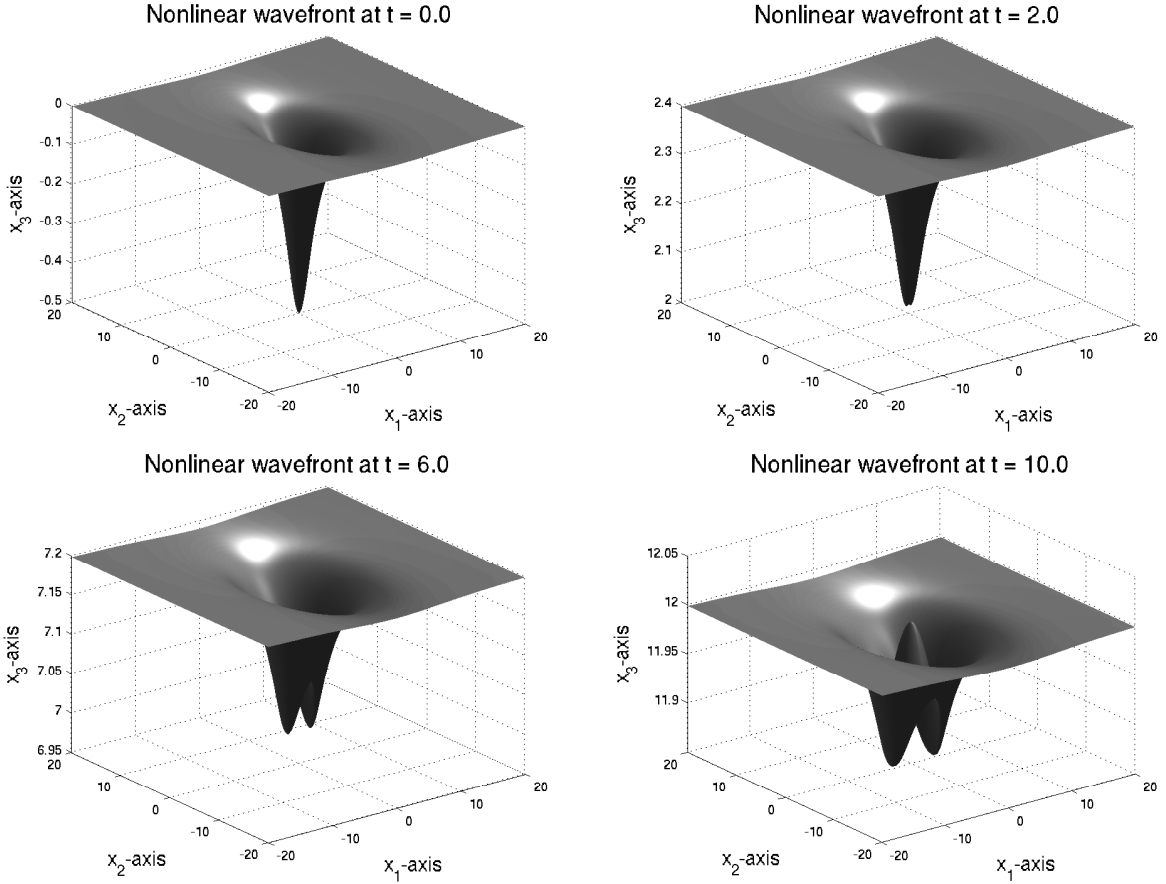


FIGURE 3. Problem 5.1: The successive positions of the nonlinear wavefront  $\Omega_t$  with an initial smooth dip which is not axisymmetric.

More precisely, the results of section 4 show that the linearly growing terms appearing in the components of the vectors  $g_1 \mathbf{u}$  and  $g_2 \mathbf{v}$  vanish under the constraint at time  $t = 0$ . Note that the choice of the initial values in section 3.3 is such that the geometric solenoidal constraint is satisfied at  $t = 0$ . Moreover, with the aid of the constrained transport technique, we are able to preserve the geometric solenoidal constraint at any time up to machine round-off error, see for e.g. Figure 6. We now proceed to give an evidence of the disappearance of the linearly growing Jordan with the aid of our numerical experiments. For this, we compute the  $L^1$  and  $L^2$  norms of the components of the vectors  $g_1 \mathbf{u}$  and  $g_2 \mathbf{v}$  as functions of time  $t$ , for a long time. If there is any Jordan mode present, the numerical values of these norms would exhibit a linear growth with time. For any grid function  $\omega$ , the norms are computed using the formulae

$$(5.4) \quad \begin{aligned} \|\omega(t)\|_{L^1} &= \Delta\xi_1 \Delta\xi_2 \sum_{i=1}^{K_1} \sum_{j=1}^{K_2} |\bar{\omega}_{i,j}(t)|, \\ \|\omega(t)\|_{L^2} &= \sqrt{\Delta\xi_1 \Delta\xi_2 \sum_{i=1}^{K_1} \sum_{j=1}^{K_2} \bar{\omega}_{i,j}(t)^2}. \end{aligned}$$

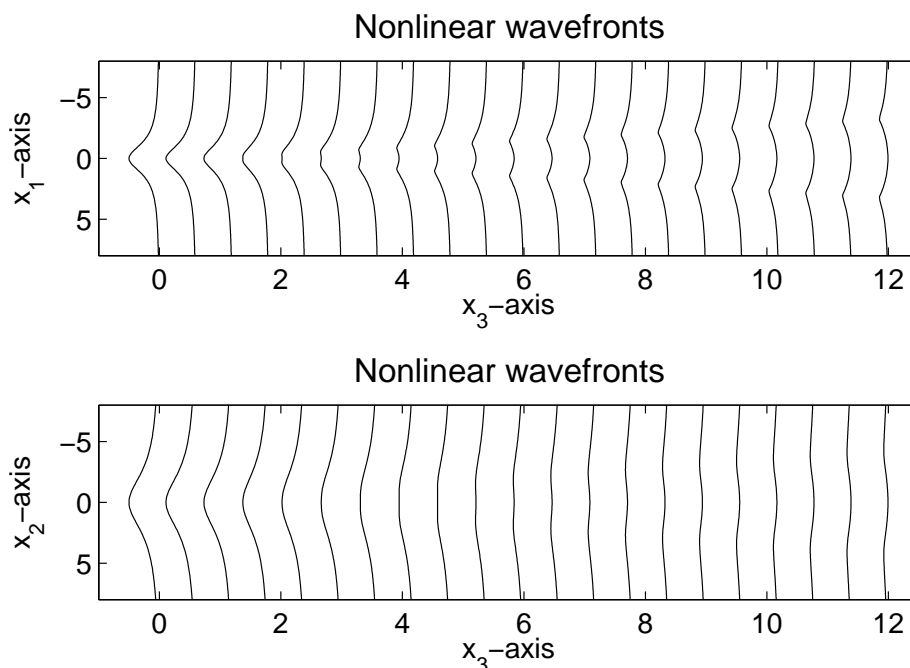


FIGURE 4. Problem 5.1: The sections of the nonlinear wavefront at times  $t = 0.0, \dots, 10.0$  with a time step 0.5. On the top: along  $x_2 = 0$  plane. Bottom: in  $x_1 = 0$  plane.

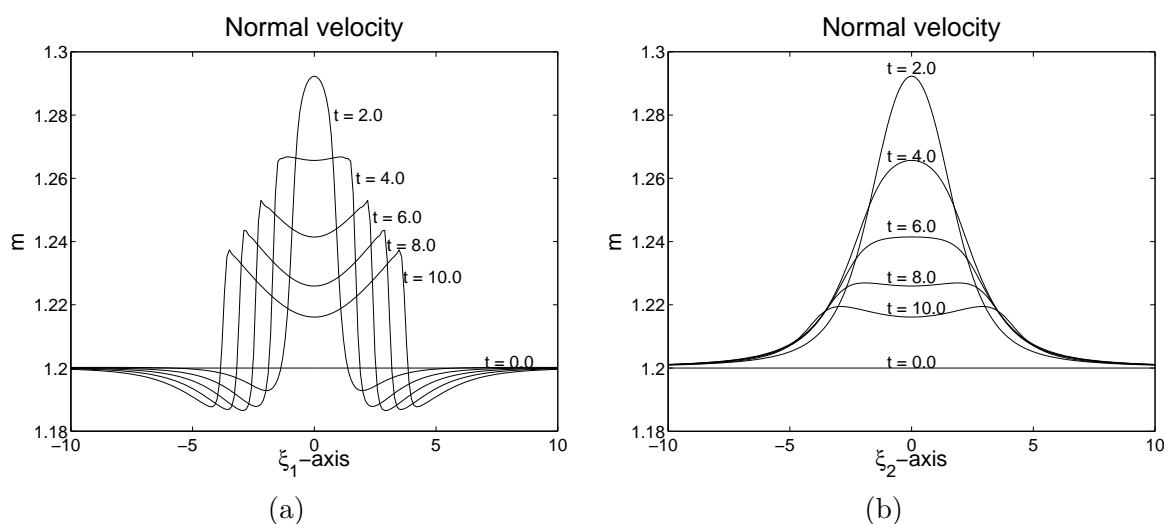


FIGURE 5. Problem 5.1: The time evolution of the normal velocity  $m$ . (a): along  $\xi_1$ -direction in the section  $\xi_2 = 0$ . (b): along  $\xi_2$ -direction in the section  $\xi_1 = 0$ .

Here  $K_1$  and  $K_2$  respectively denote the number of mesh points in  $\xi_1$ - and  $\xi_2$ -directions. In Figure 7 we give the plots of  $L^1$  and  $L^2$  norms of the components of the vectors  $g_1 \mathbf{u}$  and  $g_2 \mathbf{v}$  up to time  $t = 200$ . It is clear from the figure that there is no linear growth with time for any of these quantities.

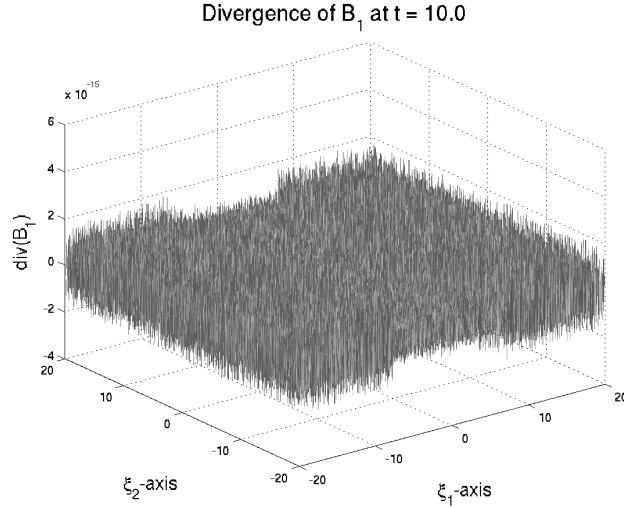


FIGURE 6. Problem 5.1: The divergence of  $\mathfrak{B}_1$  at  $t = 10.0$ . The error is of the order of  $10^{-15}$ . The vertical axis is magnified  $10^{15}$  times.

This is in conformity with the results obtained in section 4 that the Jordan mode does not appear when the geometric solenoidal constraint is satisfied.

**5.2. Corrugation Stability of a Nonlinear Wavefront.** By corrugational stability, we mean the stability of a plane front. The corrugational stability of plane shock fronts was first discussed by Gardner and Kruskal [16] in the context of magnetohydrodynamics. Whitham [39] used his theory of shock dynamics to study this problem. Anile and Russo [1] obtained an exact stability criterion for plane relativistic shock waves. The WNLRT is a very powerful method to study the corrugational stability of a nonlinear wavefront. It should be possible to use it to obtain some theoretical results, but the system being highly nonlinear, this appears to be too difficult. Therefore, we take help of numerical computations to establish the results. The extensive numerical computations by Prasad and Sangeeta [31] with 2-D WNLRT show that a planar nonlinear wavefront in 2-D is corrugationally stable, see also [25] for a related discussion of corrugation stability of a 2-D shock front.

Here we intent to study the corrugation stability of a 3-D nonlinear wavefront using WNLRT. We give two illustrations showing corrugation stability. In the first case we choose the initial front to be of a periodic shape

$$(5.5) \quad \Omega_0: x_3 = \kappa \left( 2 - \cos\left(\frac{\pi x_1}{a}\right) - \cos\left(\frac{\pi x_2}{b}\right) \right),$$

with the constants  $\kappa = 0.1, a = b = 2$ . The initial choice of the ray coordinates and the unknown variables are done as in the previous problems. The initial velocity has a constant value  $m_0 = 1.2$  throughout the front. The computational domain  $[-4, 4] \times [-4, 4]$  is divided into  $401 \times 401$  mesh points. The simulations are for  $t = 20, 40, 60$  and we have applied periodic boundary conditions everywhere.

In Figure 8 we give the surface plots of the initial wavefront  $\Omega_0$  and the wavefronts  $\Omega_t$  at times  $t = 20, 40, 60$ . The front  $\Omega_t$  moves up in the  $x_3$ -direction and has developed several kink lines. At time  $t = 20$  we can observe eight kink lines on the wavefront, of which four of them are parallel to  $x_1$ -axis and remaining four parallel to the  $x_2$ -axis. Further, we can also observe the interaction of the kink lines and the front developing complex patterns. It is to be noted that during its time

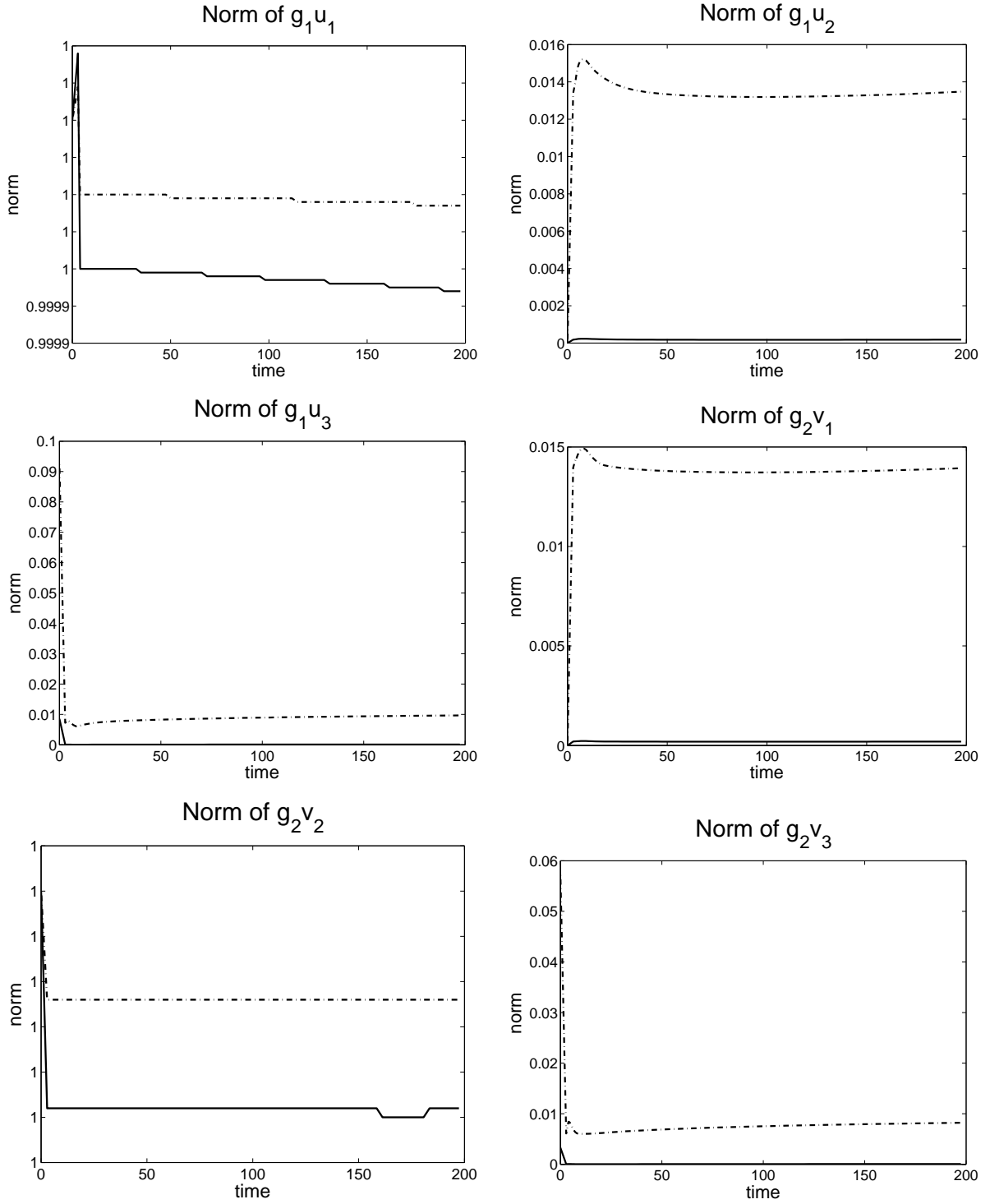


FIGURE 7. Problem 5.1:  $L^1$  and  $L^2$  norms of the components of  $g_1 \mathbf{u}$  and  $g_2 \mathbf{v}$ . Solid line represents the  $L^1$  norm and dotted line is the  $L^2$  norm.

evolution, the elevations and depressions on the front decrease, which shows that the wavefront tends to become planar leading to corrugational stability.

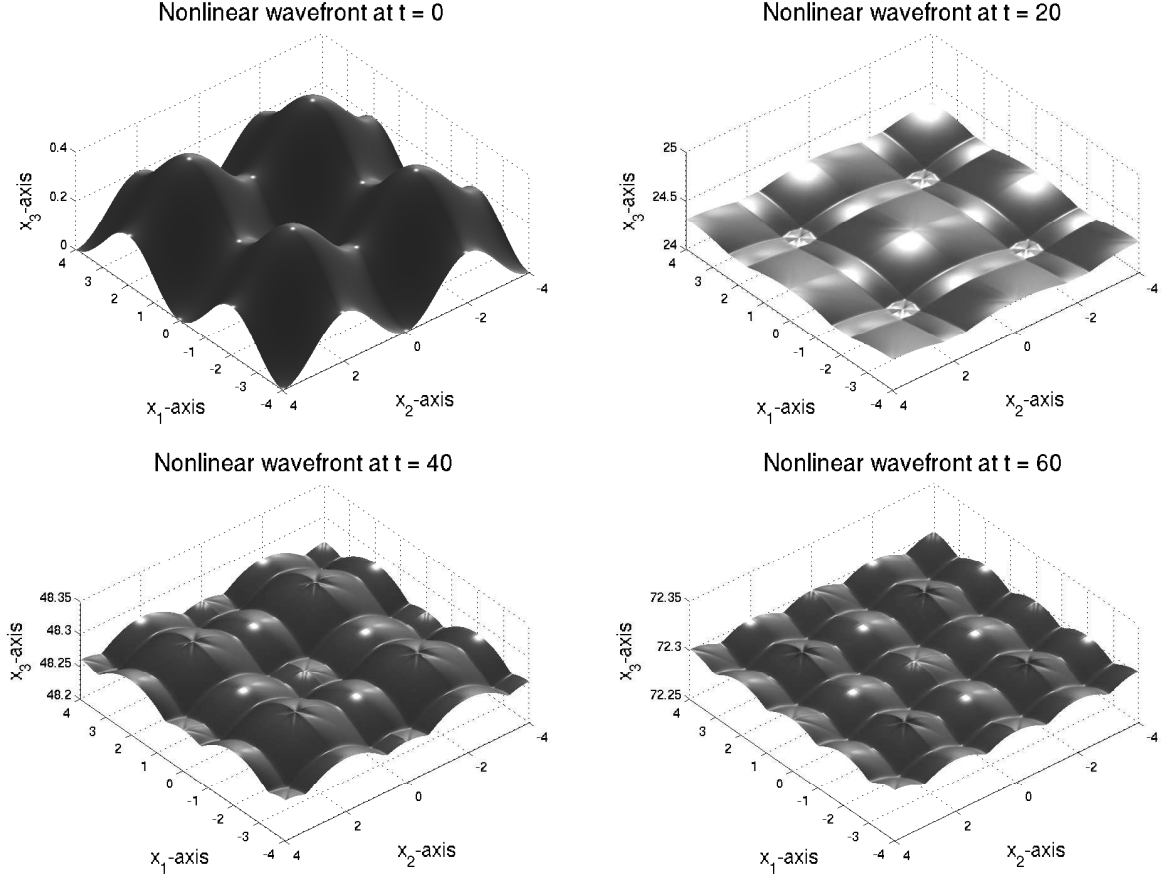


FIGURE 8. Problem 5.2: Nonlinear wavefront  $\Omega_t$  starting initially in a periodic shape with  $m_0 = 1.2$ . The front develops a complex pattern of kinks and ultimately tends to become planar.

It can be noted from Figure 8 that the wavefronts at times  $t = 40$  and  $t = 60$  show a very complex pattern of kink lines. To get a better feeling of this phenomenon, in Figure 9 we plot a zoomed portion in one period of the wavefront at time  $t = 40$ .

During its time evolution, the elevations and depressions on the front diminish, and as a result its height decreases. In order to quantify the reduction of height, we compute the maximum height of the wavefront at any time in the following way. Let us consider

$$(5.6) \quad x_{3\max}(t) = \max_{i,j} x_3(\xi_{1i}, \xi_{2j}, t), \quad x_{3\min}(t) = \min_{i,j} x_3(\xi_{1i}, \xi_{2j}, t).$$

The maximum height  $h$  is defined via

$$(5.7) \quad h(t) := x_{3\max}(t) - x_{3\min}(t).$$

In Figure 10(a) we give the plot of height versus time, which shows that  $h$  reduces with time. Hence, it can easily be seen that the wavefront tends to become planar leading to corrugational stability. Moreover, this test also shows the efficiency of the central scheme to continue the computations for

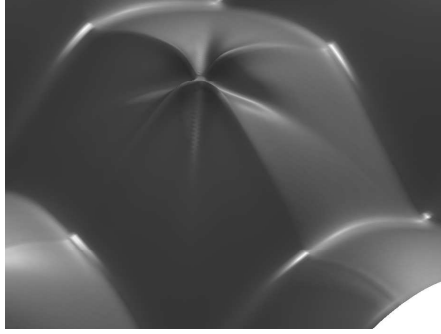


FIGURE 9. Problem 5.2: A zoomed portion of the periodic nonlinear wavefront  $\Omega_t$  in one period at time  $t = 40$ . The wavefront shows four horizontal kink curves intersecting at one point and four other kink curves in background.

a very long time. In Figure 10(b) we have plotted the divergence of  $\mathfrak{B}_1$  at time  $t = 60$ . The figure shows that the divergence of  $\mathfrak{B}_1$  is zero up to machine round-off error even for a very long time.

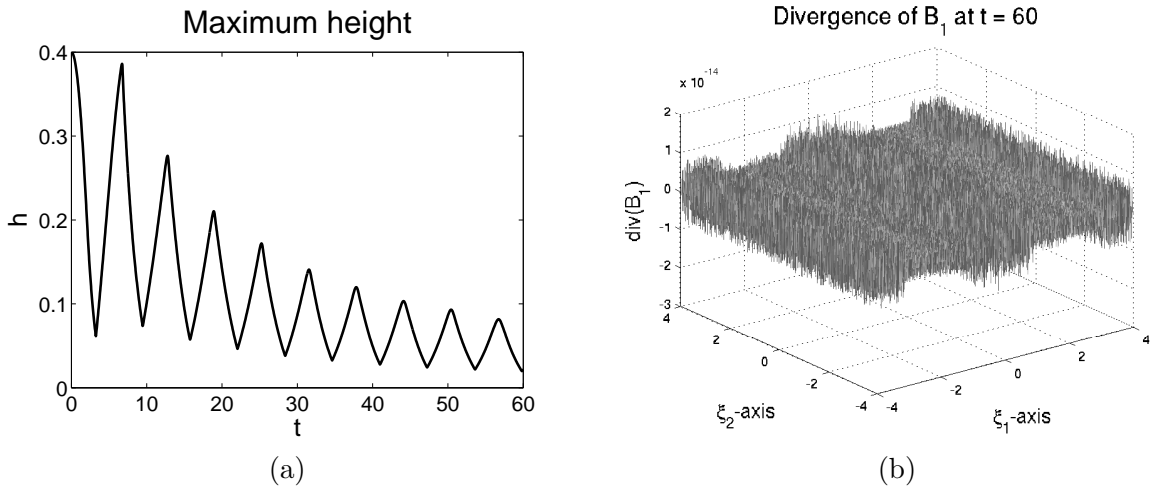


FIGURE 10. Problem 5.2: (a): time variation maximum height of the wavefront which is initially a smooth periodic pulse. (b): divergence of  $\mathfrak{B}_1$  computed at time  $t = 60$ . The vertical axis is magnified  $10^{15}$  times.

During the evolution of the wavefront  $\Omega_t$ , the normal velocity  $m$  decays to the initial mean value 1.2 along each ray. In order to show this decay, we calculate the maximum and minimum of  $m$  taken over  $(\xi_1, \xi_2)$  at any time  $t$ , i.e.

$$(5.8) \quad m_{\max}(t) = \max_{\xi_1, \xi_2} m(\xi_1, \xi_2, t), \quad m_{\min}(t) = \min_{\xi_1, \xi_2} m(\xi_1, \xi_2, t).$$

In Figure 11(a) we plot the distribution of  $m_{\max}(t), m_{\min}(t)$  with respect to time  $t$ . It can be noted that  $m_{\max}(t)$  attains a maximum value greater than  $m_{\max}(0) = 1.2$  at time  $t = 7$  almost, which is approximately the time when the kinks first appear. Similarly,  $m_{\min}(t)$  attains its first minimum value at  $t = 5$  just before the kinks form. The Figure 11(a) shows that  $m_{\max}(t)$  and  $m_{\min}(t)$  both tend to 1.2 asymptotically. From Figure 11(b) we observe that  $m_{\max}(t) - m_{\min}(t) \rightarrow 0$  as  $t \rightarrow \infty$ , confirming corrugational stability.

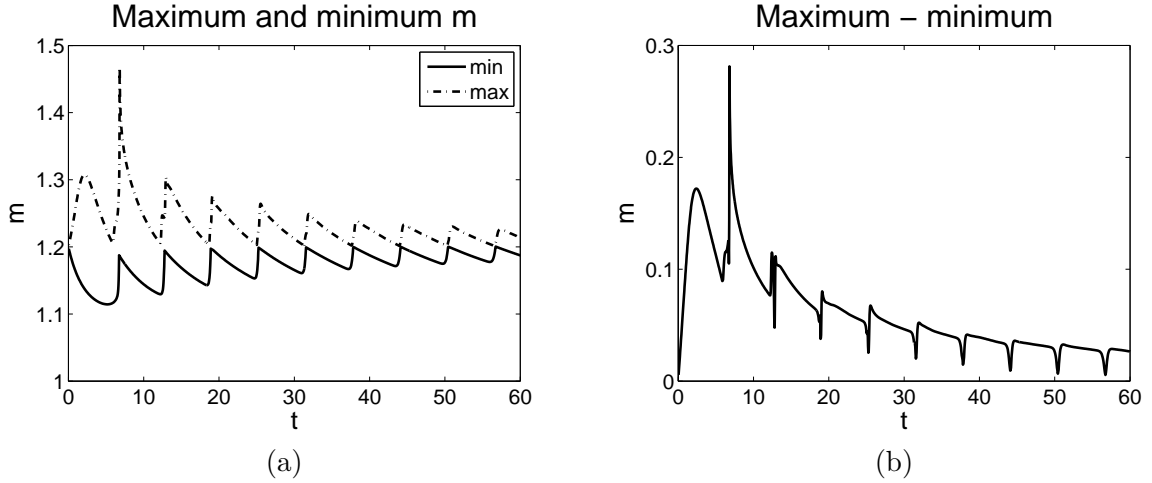


FIGURE 11. Problem 5.2: (a): variation of  $m_{\max}(t)$  and  $m_{\min}(t)$  with time from  $t = 0$  to  $t = 60$ . (b): the difference  $m_{\max}(t) - m_{\min}(t)$  tends to zero as  $t \rightarrow \infty$ .

We give another illustration of corrugation stability as follows. In Figure 7 we have given the plots of  $L^1$  and  $L^2$  norms of the components of the vectors  $g_1 \mathbf{u}$  and  $g_2 \mathbf{v}$  for the problem in section 5.1. The plots in Figure 7 show that these norms tend to a constant value as time  $t \rightarrow \infty$ . This is because, as  $t \rightarrow \infty$ , the front becomes planar and as a result  $g_1 \mathbf{u}$  and  $g_2 \mathbf{v}$  assume constant values.

**5.3. Converging Wavefront Initially in the Shape of a Circular Cylinder.** Next we present the results of simulation of a cylindrically converging wavefront. The motivation for this test problem is the one considered by Schwendeman [34]. The initial geometry of the wavefront is a portion of a circular cylinder of radius two units, i.e.

$$(5.9) \quad x_1^2 + x_2^2 = 4, \quad -\frac{\pi}{2} \leq x_3 \leq \frac{\pi}{2}.$$

Initially the ray coordinates  $(\xi_1, \xi_2)$  are chosen as  $\xi_1 = x_3$  and  $\xi_2 = \theta$ , where  $\theta$  is the azimuthal angle. Therefore, the initial wavefront  $\Omega_0$  given in (5.9) can be expressed in a parametric form

$$(5.10) \quad x_1 = 2 \cos \xi_2, \quad x_2 = 2 \sin \xi_2, \quad x_3 = \xi_1,$$

where the range of variation of  $\xi_1$  and  $\xi_2$  are taken as

$$(5.11) \quad -\frac{\pi}{2} \leq \xi_1 \leq \frac{\pi}{2}, \quad 0 \leq \xi_2 \leq 2\pi.$$

The formulation of the initial values of the unknown variables is done using the representation (5.10). As a result of this particular choice of the ray coordinates  $(\xi_1, \xi_2)$ , the unit normal to  $\Omega_0$  is  $\mathbf{n}_0 = (-\cos \xi_2, \sin \xi_2, 0)$ , which points inward and hence the front converges. Further, if we choose a uniform distribution of  $m$  on  $\Omega_0$ , the front  $\Omega_t$  at any successive time  $t$  will remain as a circular cylinder with no interesting geometrical features for  $t > 0$ . Hence, the initial distribution of the normal velocity  $m$  is taken as

$$(5.12) \quad m_0(\xi_1, \xi_2) = 1.2 + \alpha \cos(\nu \xi_2)$$

with the parameter values  $\alpha = 0.05$  and  $\nu = 8$ .

The computational domain  $[-\pi/2, \pi/2] \times [0, 2\pi]$  is divided into  $301 \times 601$  cells. The simulations are done up to a time  $t = 1.0$  and we have applied periodic boundary conditions for  $\xi_2$  and non-reflecting boundary conditions for  $\xi_1$ .

In Figure 12 we give the plots of the initial wavefront  $\Omega_0$  and the successive wavefronts  $\Omega_t$  at times  $t = 0.2, 0.4, 0.6, 0.8, 1.0$ . The wavefronts are coloured using the variation of the normal velocity  $m$  with the colour-bar on the right indicating the values of  $m$ . Note that the initial normal velocity  $m_0$  in (5.12) has a periodic variation with respect to  $\xi_2$  with a maximum value 1.25 and a minimum value 1.15. Those portions of the front where  $m_0$  has maximum value moves inwards faster and it results in a distortion of the circular shape of  $\Omega_0$ . Vertical kink lines are starting to form on the wavefront at time  $t = 0.8$ , and as a result the front finally tends to assume the shape of a polygonal cylinder.

In order to show the rate of convergence with respect to time  $t$ , we compute the maximum and minimum radius  $r$  and velocity  $m$  at a section of the wavefront cut off by the plane  $x_3 = 0$ . In Figure 13(a)-(b) we give the plots of these quantities versus time. From the figure we can notice a sudden increase in the maximum velocity after  $t = 0.6$ . On the other hand, the minimum of the normal velocity shows a gradual increase with time in Figure 13(a). It is to be noted that we should not continue the computations indefinitely as  $m - 1$  becomes too large for the WNLRT to be valid. From the plot in Figure 13(b) we can infer a linear decay of the maximum and minimum radial distance over time.

Finally, in Figure 14(a) we give the plot of the distribution of  $m$  with respect to  $\xi_2$  from  $t = 0$  to  $t = 1.0$  with a time step of 0.1 and in Figure 14(b), the discrete divergence of  $\mathfrak{B}_1$ . Due to symmetry, in Figure 14(a) we have plotted  $m$  only in the range  $[0, \pi/2]$ . We notice that the difference  $m_{\max}(t) - m_{\min}(t)$  oscillates significantly. However, this oscillation is quite small at time  $t = 0.8$  due to the fact that  $m_{\max}$  decreases and  $m_{\min}$  increases. We can see that four shocks are trying to form in  $m$  at  $t = 1.0$  in the interval  $[0, \pi/2]$ . These shocks in turn corresponds to the kink lines on the wavefront. The plot in Figure 14(b) gives the divergence of  $\mathfrak{B}_1$  at time  $t = 1.0$ . The discrete divergence is zero value up to machine round-off error, despite a very strong convergence of the rays.

**5.4. Spherically Converging Wavefront.** In this test problem we consider the propagation of a spherically converging wavefront. The motivation for this problem is an analogous case studied by Schwendeman in [34]. The initial geometry of the wavefront is a sphere of radius 2. The ray coordinates are chosen to be  $\xi_1 = \pi - \phi$ ,  $\xi_2 = \theta$ , where  $\theta$  is the azimuthal angle and  $\phi$  is the polar angle. The parametric representation of the initial wavefront  $\Omega_0$  is

$$(5.13) \quad x_1 = 2 \sin \xi_1 \cos \xi_2, \quad x_2 = 2 \sin \xi_1 \sin \xi_2, \quad x_3 = -2 \cos \xi_1.$$

In order to avoid the singularities at  $\phi = 0$  and  $\phi = \pi$ , we remove this points. Therefore, our computational domain is  $[\pi/15, 14\pi/15] \times [0, 2\pi]$ . We choose the initial velocity distribution as

$$(5.14) \quad m_0(\xi_1, \xi_2) = 1.2 + \alpha \cos(\nu_1 \xi_1) \cos(\nu_2 \xi_2)$$

with  $\alpha = 0.05, \nu_1 = 4, \nu_2 = 8$ .

We divide the computational domain into  $301 \times 601$  mesh points. The computations are done up to time  $t = 0.85$ . We have applied absorbing boundary conditions at  $\xi_1 = \pi/15$  and  $\xi_1 = 14\pi/15$  and periodic boundary conditions at  $\xi_2 = 0$  and  $\xi_2 = 2\pi$ .

The plots of the wavefronts at times  $t = 0.0, 0.5, 0.75, 0.85$  are given in Figure 15. The wavefronts are coloured using the variation of the normal velocity  $m$  with the colour-bar on the right indicating the values of  $m$ . It can be observed from the figure that as the front starts focusing it develops several kink curves and its shape gets distorted. The final shape of the wavefront is a polygon with facets.

To show the intensity of wavefront focusing we compute the maximum and minimum radial distance  $r$  of the points on  $\Omega_t$  from the centre  $(0, 0, 0)$  as a function of time. We also calculate the maximum and minimum of the normal velocity  $m$  with respect to time. Here we take the maximum

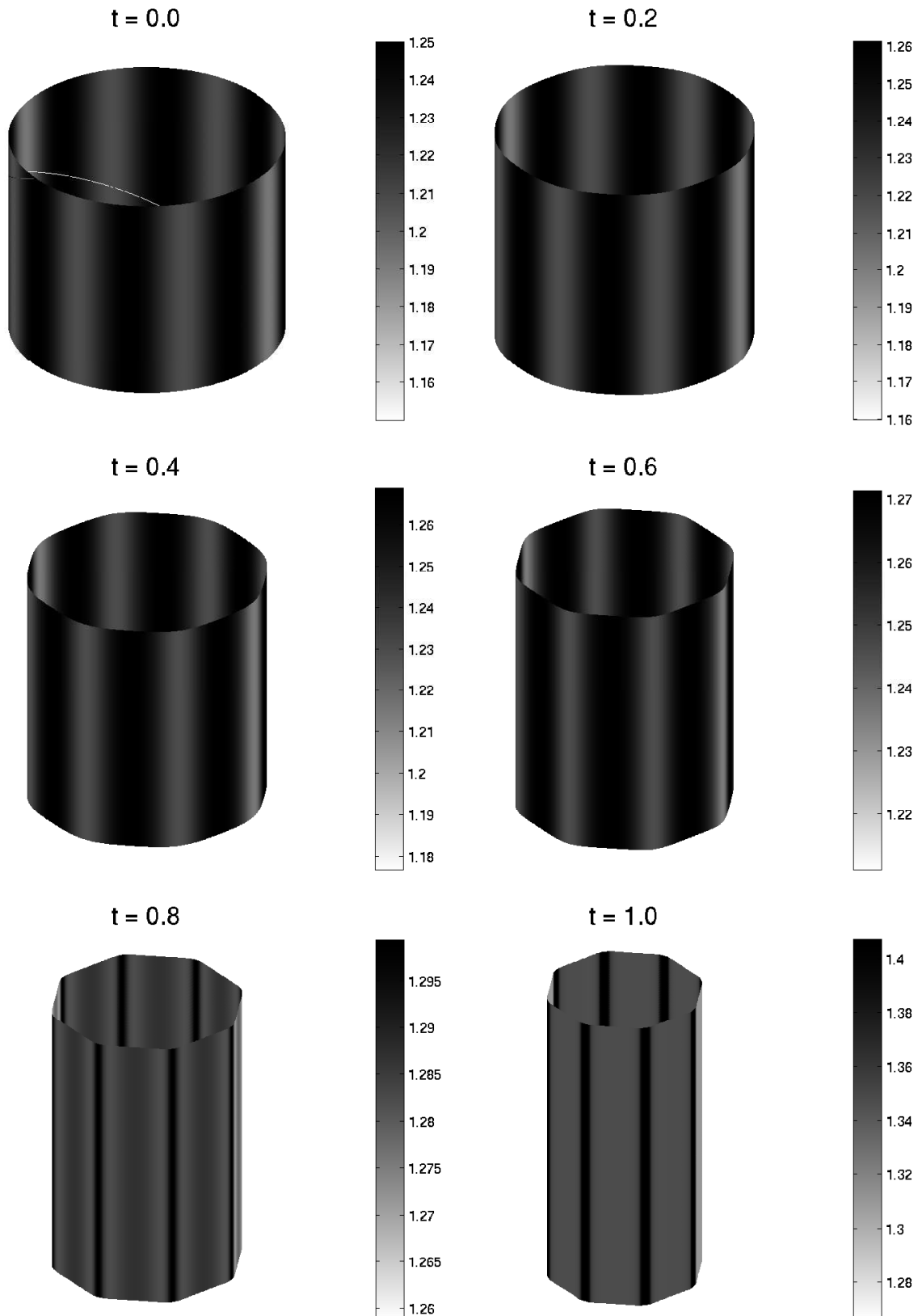


FIGURE 12. Problem 5.3: Cylindrically converging wavefronts at times  $t = 0.0, 0.2, 0.6, 0.8, 1.0$ . The initial wavefront is in the shape of a circular cylinder. The colour bar on the right hand side indicates the intensity of the normal velocity  $m$ .

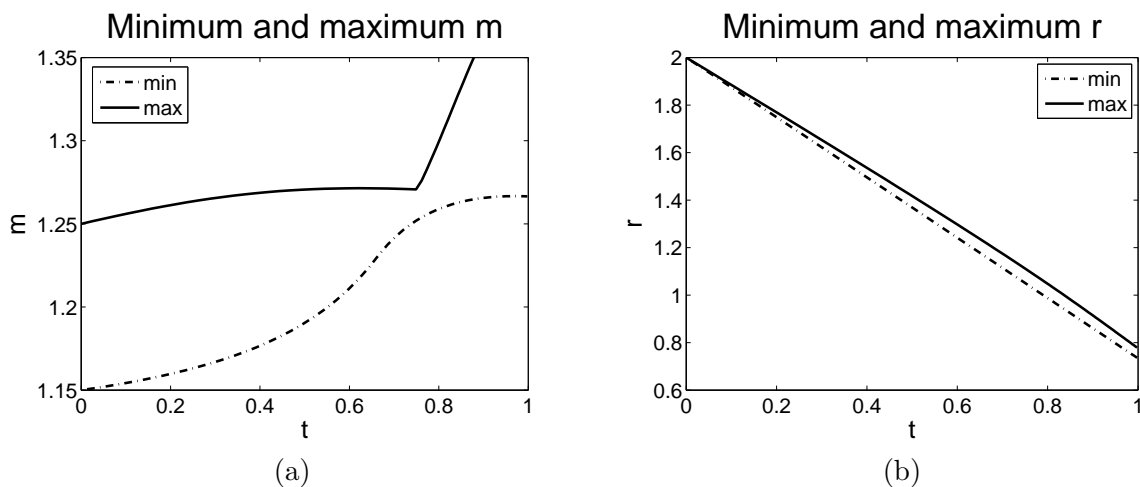


FIGURE 13. Problem 5.3: (a): time variation of maximum and minimum  $m$  at the section  $x_3 = 0$ . (b): distribution of maximum and minimum radial distance with time.

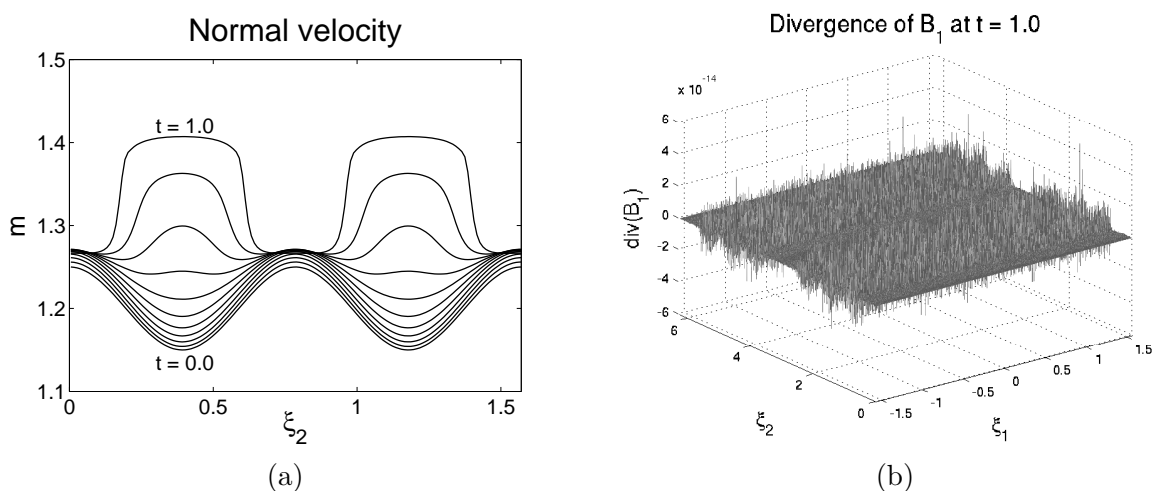


FIGURE 14. Problem 5.3: (a): variation of  $m$  with respect to  $\xi_2$  in the interval  $[0, \pi/2]$  from time  $t = 0.0$  to  $t = 1.0$ . (b):  $\text{div}(\mathfrak{B}_1)$  at time  $t = 1.0$ . The vertical axis is magnified  $10^{14}$  times.

and minimum over the whole surface of the wavefront  $\Omega_t$ . In Figure 16(a)-(b) we give the plots of these quantities versus time. From the plot in Figure 16(a) we can observe that the radial distance  $r$  reduces almost linearly in time. The maximum and minimum radii reduce to more than half of their initial value 2 at  $t = 0$ . The plot of normal velocity in Figure 16(b) shows a sharp increase in the maximum  $m$  at around  $t = 0.6$ , indicating the formation of kinks. The minimum  $m$  has a gradual increase. The variation of minimum and maximum  $m$  are qualitatively similar to those of the cylindrically converging wavefront problem in section 5.3.

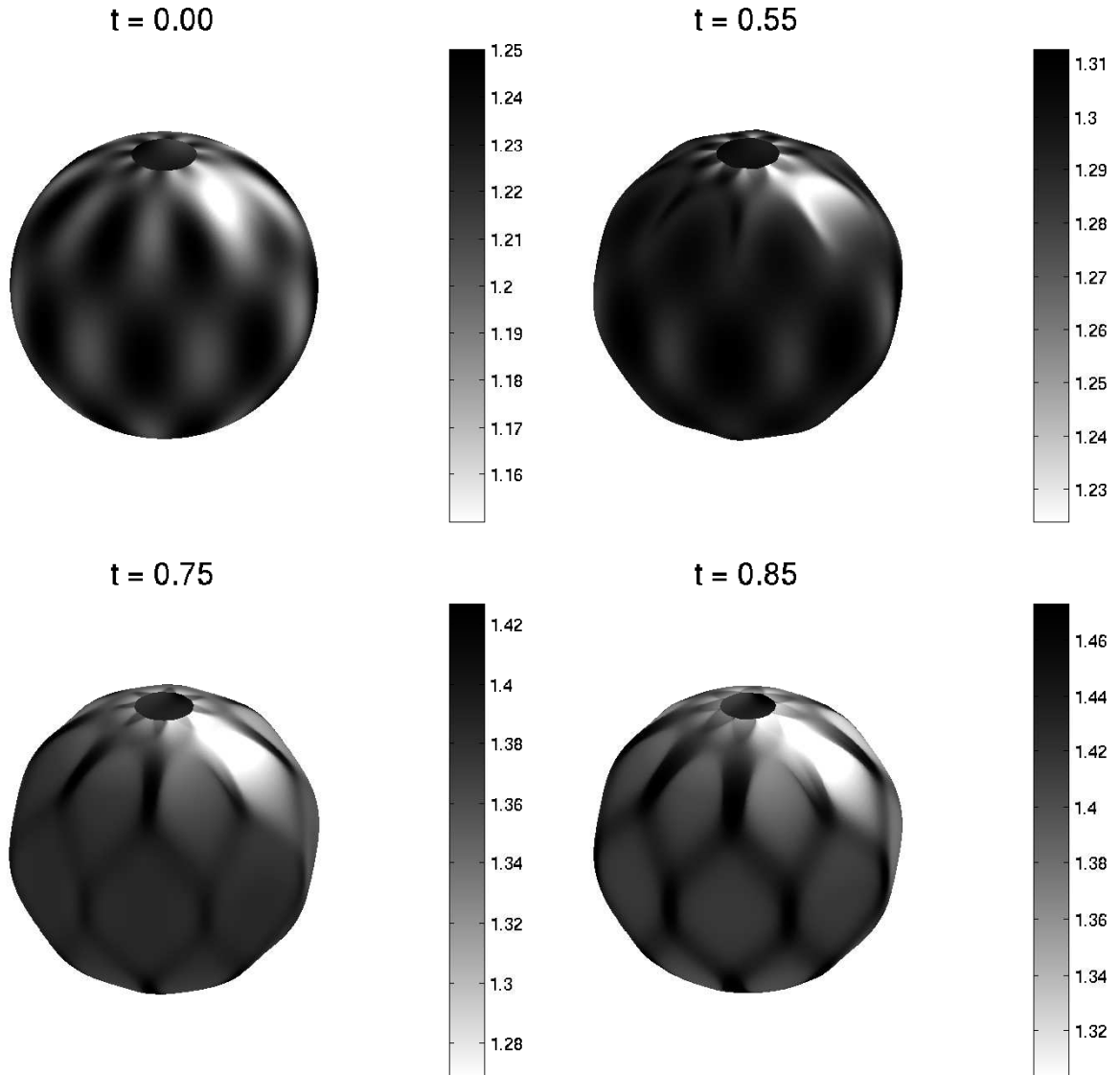


FIGURE 15. Problem 5.4: Spherically focusing wavefronts at times  $t = 0.0, 0.5, 0.75, 0.85$ . The colour bar on the right represents the distribution of  $m$ .

#### ACKNOWLEDGEMENTS

The author sincerely thank Prof. Phoolan Prasad and Prof. Maria Lukáčová for their constant encouragement and invaluable support. He also wish to thank the Council of Scientific and Industrial Research (CSIR), Government of India for supporting his research under grant-09/079(2084)/2006-EMR-1. The Department of Mathematics is partially supported by the UGC under DSA-SAP, Phase IV.

#### REFERENCES

- [1] A. M. Anile and G. Russo. Corrugation stability for plane relativistic shock waves. *Phys. Fluids*, 29:2847–2852, 1986.

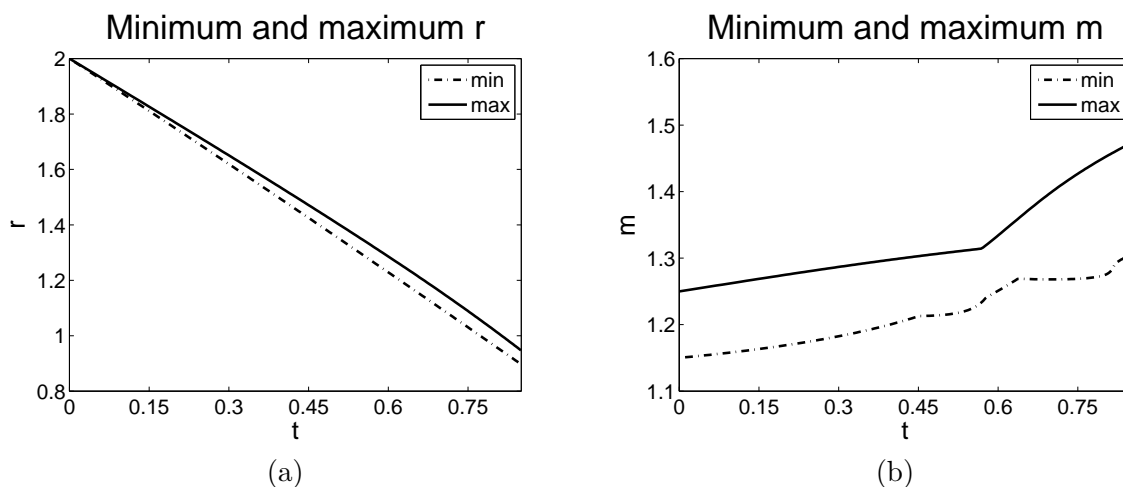


FIGURE 16. Problem 5.4: Spherically converging wavefront. (a): time distribution of the maximum and minimum  $r$ . (b): maximum and minimum  $m$ .

- [2] K. R. Arun, M. Lukáčová-Medvidová, P. Prasad, and S. V. Raghurama Rao. An application of 3-D kinematical conservation laws: propagation of a three dimensional wavefront. Technical report, Department of Mathematics, Indian Institute of Science, Bangalore, 2009. To appear in SIAM. J. Appl. Math.
- [3] K. R. Arun and P. Prasad. 3-D kinematical conservation laws (KCL): evolution of a surface in  $\mathbb{R}^3$ -in particular propagation of a nonlinear wavefront. *Wave Motion*, 46:293–311, 2009.
- [4] K. R. Arun and P. Prasad. Eigenvalues of kinematical conservation laws (KCL) based 3-D weakly nonlinear ray theory (WNLRT). Technical report, Department of Mathematics, Indian Institute of Science, Bangalore, 2009. To appear in Appl. Math. comput.
- [5] D. S. Balsara and D. S. Spicer. A staggered mesh algorithm using high order Godunov fluxes to ensure solenoidal magnetic fields in magnetohydrodynamic simulations. *J. Comput. Phys.*, 149:270–292, 1999.
- [6] S. Baskar and P. Prasad. Kinematical conservation laws applied to study geometrical shapes of a solitary wave. In S. Sajjadi and J. Hunt, editors, *Wind over Waves II: Forecasting and Fundamentals*, pages 189–200. Horwood Publishing Ltd, 2003.
- [7] S. Baskar and P. Prasad. Propagation of curved shock fronts using shock ray theory and comparison with other theories. *J. Fluid Mech.*, 523:171–198, 2005.
- [8] S. Baskar and P. Prasad. Formulation of the sonic boom problem by a maneuvering aerofoil as a one parameter family of cauchy problems. *Proc. Indian Acad. Sci. Math. Sci.*, 116:97–119, 2006.
- [9] S. Benzoni-Gavage and D. Serre. *Multidimensional hyperbolic partial differential equations*. Oxford Mathematical Monographs. The Clarendon Press Oxford University Press, Oxford, 2007. First-order systems and applications.
- [10] G. Boillat. Symétrisation des systèmes d'équations aux dérivées partielles avec densité d'énergie convexe et contraintes. *C. R. Acad. Sci. Paris*, 295:551–554, 1982.
- [11] G. Boillat and A. Muracchini. On the symmetric conservative form of Landau's superfluid equations. *Z. Angew. Math. Phys.*, 35:282–288, 1984.
- [12] F. Bouchut, S. Jin, and X. Li. Numerical approximations of pressureless and isothermal gas dynamics. *SIAM J. Num. Anal.*, 41:135–158, 2003.
- [13] W. Dai and P. R. Woodward. A simple finite difference scheme for multidimensional magnetohydrodynamical equations. *J. Comput. Phys.*, 142:331–369, 1998.
- [14] B. Enquist and O. Runborg. Multi-phase computations in geometrical optics. *J. Comp. Appl. Math.*, 74:175–192, 1996.
- [15] S. A. E. G. Falle and T. W. Hartquist. Generation of density inhomogeneties by magnetohydrodynamic waves. *Mon. Not. R. Astron. Soc.*, 329:195–203, 2002.
- [16] C. S. Gardner and M. D. Kruskal. Stability of plane magnetohydrodynamic shocks. *Phys. Fluids.*, 7:700–706, 1964.
- [17] M. B. Giles, P. Prasad, and R. Ravindran. Conservation forms of equations of three dimensional front propagation. Technical report, Department of Mathematics, Indian Institute of Science, Bangalore, 1995.

- [18] W. D. Henshaw, N. F. Smyth, and D. W. Schwendeman. Numerical shock propagation using geometrical shock dynamics. *J. Fluid Mech.*, 171:519–545, 1986.
- [19] G.-S. Jiang and C.-W. Shu. Efficient implementation of weighted ENO schemes. *J. Comput. Phys.*, 126:202–228, 1996.
- [20] B. L. Keyfitz and H. C. Kranzer. A system of nonstrictly hyperbolic conservation laws arising in elasticity theory. *Arch. Rational Mech. Anal.*, 72:219–241, 1980.
- [21] D. J. Korchinski. *Solutions of a Riemann problem for a  $2 \times 2$  system of conservation laws possessing no classical weak solution*. PhD thesis, Adelphi University, 1977.
- [22] A. Kurganov and E. Tadmor. New high-resolution central schemes for nonlinear conservation laws and convection-diffusion equations. *J. Comput. Phys.*, 160:241–282, 2000.
- [23] R. J. LeVeque. The dynamics of pressureless dust clouds and delta waves. *J. Hyper. Diff. Equat.*, 1:315–327, 2004.
- [24] T.-T. Li and Y.-J. Peng. Cauchy problem for weakly linearly degenerate hyperbolic systems in diagonal form. *Nonlinear Anal.*, 55:937–949, 2003.
- [25] A. Monica and P. Prasad. Propagation of a curved weak shock. *J. Fluid Mech.*, 434:119–151, 2001.
- [26] K. W. Morton, P. Prasad, and R. Ravindran. Conservation forms of nonlinear ray equations. Technical report, Department of Mathematics, Indian Institute of Science, Bangalore, 1992.
- [27] S. Pennisi. A new approach to constrained systems with convex extension. *Note di Matematica*, 16:173–187, 1996.
- [28] P. Prasad. A nonlinear ray theory. *Wave Motion*, 20:21–31, 1994.
- [29] P. Prasad. *Nonlinear Hyperbolic Waves in Multi-dimensions*. Chapman and Hall/CRC, London, 2001.
- [30] P. Prasad. Ray theories for hyperbolic waves, kinematical conservation laws (KCL) and applications. *Indian J. Pure Appl. Math.*, 38:467–490, 2007.
- [31] P. Prasad and K. Sangeeta. Numerical simulation of converging nonlinear wavefronts. *J. Fluid Mech.*, 385:1–20, 1999.
- [32] J. A. Rossmannith. An unstaggered high-resolution constrained transport method for magnetohydrodynamic flows. *SIAM J. Sci. Comp.*, 28:1766–1797, 2006.
- [33] D. Ryu, F. Miniati, T. W. Jones, and A. Frank. A divergence-free upwind code for multidimensional magnetohydrodynamic flow. *Astrophys. J.*, 509:244–255, 1998.
- [34] D. W. Schwendeman. A new numerical method for shock wave propagation based on geometrical shock dynamics. *Proc. Roy. Soc. London Ser. A*, 441:331–341, 1993.
- [35] D. W. Schwendeman. On converging shock waves of spherical and polyhedral form. *J. Fluid Mech.*, 454:365–386, 2002.
- [36] C.-W. Shu. Total-variation-diminishing time discretizations. *SIAM J. Sci. Stat. Comput.*, 9:1073–1084, 1988.
- [37] B. Sturtevant and V. A. Kulkarny. The focusing of weak shock waves. *J. Fluid Mech.*, 73:651–671, 1976.
- [38] G. B. Whitham. A new approach to problems of shock dynamics part 1. Two dimensional problem. *J. Fluid Mech.*, 2:146–171, 1957.
- [39] G. B. Whitham. *Linear and Nonlinear Waves*. John Wiley, New York, 1974.
- [40] H. Yang. Riemann problems for a class of coupled hyperbolic systems of conservation laws. *J. Differential Equations*, 159:447–484, 1999.

DEPARTMENT OF MATHEMATICS, INDIAN INSTITUTE OF SCIENCE, BANGALORE - 560012, INDIA.  
 E-mail address: arunkr@math.iisc.ernet.in